UNIVERSITY OF ICELAND

Ph.D. Dissertation
in Chemistry

Saddle Point Search Methods for Calculations of Excited Electronic States

Yorick Leonard Adrian Schmerwitz

September 2024

FACULTY OF PHYSICAL SCIENCES

Saddle Point Search Methods for Calculations of Excited Electronic States

Yorick Leonard Adrian Schmerwitz

Dissertation submitted in partial fulfillment of a
Philosophiae Doctor degree in Chemistry

Ph.D. Committee
Hannes Jónsson
Gianluca Levi
Elvar Örn Jónsson
Philipp Hansmann

Opponents
Neepa T. Maitra
Peter Malcolm Wallace Gill

Faculty of Physical Sciences
School of Engineering and Natural Sciences
University of Iceland
Reykjavík, September 2024

Saddle Point Search Methods for Calculations of Excited Electronic States

(Saddle Point Search Methods for Excited States)

Dissertation submitted in partial fulfillment of a *Ph.D.* degree in Chemistry

Copyright © 2024 Yorick Leonard Adrian Schmerwitz
All rights reserved

Faculty of Physical Sciences
School of Engineering and Natural Sciences
University of Iceland
Dunhaga 5
107 Reykjavík
Iceland

Telephone: 525-4000

Bibliographic information:
Yorick Leonard Adrian Schmerwitz, 2024, *Saddle Point Search Methods for Calculations of Excited Electronic States*, Ph.D.Dissertation, Faculty of Physical Sciences, University of Iceland, 176 pp.

Author ORCID: 0000-0001-6277-0359
ISBN: 978-9935-9768-7-1

Printing: Háskólaprent
Reykjavík, Iceland, September 2024

Abstract

Variational density functional calculations provide an improved description of electronic excitations with large change of the electron density compared to the frequently used adiabatic linear-response time-dependent density functional theory (TDDFT), as the orbitals are variationally optimized for the excited states. However, the fact that excited states are typically saddle points on the surface describing the variation of the energy of the system as a function of the electronic degrees of freedom requires identification of the directions along which the energy has to be maximized. A novel direct optimization generalized mode following approach (DO-GMF) is introduced that converges on an n^{th}-order saddle point by inverting the components of the gradient in the direction of the eigenvectors corresponding to the n lowest eigenvalues of the electronic Hessian matrix. This approach has the distinct advantages of inherently avoiding variational collapse to the ground state without additional methods and following a chosen excited state by its saddle point order through molecular configurations where the symmetry of the single determinant wave function is broken. It thereby makes it possible to calculate challenging charge transfer excitations, avoided crossings and conical intersections where other state-specific methods tend to fail. Additional implementation challenges introduced by Perdew-Zunger self-interaction correction are overcome by extending the DO-GMF method. The method is demonstrated in calculations of potential energy curves for the ethene and dihydrogen molecules. Results of calculations are presented for challenging charge transfer excitations in organic molecules and the negatively charged nitrogen-vacancy defect in diamond.

Ágrip

Hnikareglureikningar með þéttnifellum gefa betri lýsingu á rafeindaörvunum þegar rafeindaþéttnin breytist verulega heldur en sú aðferð sem nú er oftast notuð og byggist á tímaháðum þéttnifellareikningum með adíabatnálgun og línulegri svörun (TDDFT). Lögun orkuyfirborða sem nálgast hvort annað, so sem við skörunarforðun og keilusniðsmót, er einnig betur lýst því svigrúmin eru bestuð fyrir örvuðu ástöndin. En, örvuð ástönd eru yfirleitt söðulpunktar á orkuyfirborðinu sem sýnir hvernig orka kerfisins er háð frelsisgráðum rafeindanna og því er nauðsynlegt að finna þær stefnur þar sem hámarka þarf orkuna. Nýstárleg aðferð sem byggist á beinni bestun og útvíkkaðri háttafylgni (DO-GMF) er sett fram til að ná samleitni á n-tu gráðu söðulpunkta með því að snúa við þeim þáttum stigilsins sem eru í stefnu eiginvigra lægstu n eigingilda Hessian fylkisins. Þessi aðferð hefur þá kosti að engin viðbótarskilyrði þarf til að forða reikningunum frá því að hrapa niður á grunnástandið vegna þess að söðulpunkti af tiltekinni gráðu er fylgt í gegnum atóm upprāðanir þar sem samhverfa einákveðu bylgjufallsins brotnar. Þar með getur aðferðin lýst erfiðum hleðslufærslu örvunum, skörunarforðun og keilusniðsmótum þar sem aðrar ástandsmiðaðar aðferðir eiga það til að bregðast. Viðbótar áskoranir sem koma fram þegar Perdew-Zunger sjálfvíxlverkunarleiðréttting er gerð hafa verið leystar með því að útvíkka beinu bestunaraðferðina. Sýnt er fram á kosti aðferðinnar í reikningum á eþen og vetnissameindum. Niðurstöðum úr reikningum á vandasömum hleðslufærsluörvunum í lífrænum sameindum sem og neikvætt hlaðinni köfnunarefnis-eyðuveilu í demanti er lýst.

Preface

The research presented in this thesis was completed in the research group of Professor Hannes Jónsson at the University of Iceland between April 2020 and September 2024.

Table of Contents

List of Figures

List of Tables

List of Publications

Article I: **Yorick L. A. Schmerwitz**, Gianluca Levi, Hannes Jónsson, 2023, Calculations of Excited Electronic States by Converging on Saddle Points Using Generalized Mode Following. *Journal of Chemical Theory and Computation*, Vol. 19, Issue 12, pp. 3634–3651. Accessed at `https://pubs.acs.org/doi/abs/10.1021/acs.jctc.3c00178`. Yorick Leonard Adrian Schmerwitz came up with the generalization of the algorithm used and described in the article, implemented the algorithm, performed calculations, created figures, and wrote the article.

Article II: **Yorick L. A. Schmerwitz**, Nuria U. Ollé, Gianluca Levi, Hannes Jónsson, 2024, Saddle Point Search Algorithms for Variational Density Functional Calculations of Excited Electronic States with Self-Interaction Correction. *Proceedings of the Platform for Advanced Scientific Computing Conference*, pp. 1–10. Accessed at `https://dl.acm.org/doi/10.1145/3659914.3659933`. Yorick Leonard Adrian Schmerwitz came up with the extension of the algorithm used and described in the manuscript, implemented the algorithm, performed calculations, created figures, and wrote the article.

Article III: **Yorick L. A. Schmerwitz**, Aleksei V. Ivanov, Elvar Ö. Jónsson, Hannes Jónsson, Gianluca Levi, 2022, Variational Density Functional Calculations of Excited States: Conical Intersection and Avoided Crossing in Ethylene Bond Twisting. *The Journal of Physical Chemistry Letters*, Vol. 13, Issue 18, pp. 3990–3999. Accessed at `https://pubs.acs.org/doi/10.1021/acs.jpclett.2c00741`. Yorick Leonard Adrian Schmerwitz performed calculations, created figures, and wrote the article.

Article IV: Elli Selenius, Alec E. Sigurðarson, **Yorick L. A. Schmerwitz**, Gianluca Levi, 2024, Orbital-Optimized Versus Time-Dependent Density Functional Calculations of Intramolecular Charge Transfer Excited States. *Journal of Chemical Theory and Computation*, Vol. 20, Issue 9, pp. 3809–3822. Accessed at `https://pubs.acs.org/doi/10.1021/acs.jctc.3c01319`. Yorick Leonard Adrian Schmerwitz implemented the algorithm used in the article and helped with calculations and writing the manuscript.

Article V: Aleksei V. Ivanov, **Yorick L. A. Schmerwitz**, Gianluca Levi, Hannes Jónsson, 2023, Electronic excitations of the charged nitrogen-vacancy center in diamond obtained using time-independent variational density functional calculations. *SciPost Physics*, Vol. 15, Issue 1, p. 009. Accessed at `https://scipost.org/10.21468/SciPostPhys.15.1.009-update-1/`. Yorick Leonard Adrian Schmerwitz helped with calculations and writing the article.

Abbreviations

DFT	density functional theory
DO	direct optimization
DO-GMF	direct optimization generalized mode following
DO-MOM	direct optimization maximum overlap method
FD	finite difference
GGA	generalized gradient approximation
GMF	generalized mode following
HF	Hartree-Fock
HK	Hohenberg-Kohn
HOMO	highest occupied molecular orbital
KS	Kohn-Sham
KS-DFT	Kohn-Sham density functional theory
L-B	limited-memory Bofill
L-BFGS	limited-memory Broyden-Fletcher-Goldfarb-Shanno
LDA	local density approximation
L-P	limited-memory Powell
L-SR1	limited-memory symmetric rank 1
LUMO	lowest unoccupied molecular orbital
LCAO	linear combination of atomic orbitals
MO	molecular orbital
MFT	mean-field theory
MMF	minimum mode following
oo	occupied-occupied
ov	occupied-virtual
PW	plane wave
QN	quasi-Newton
SIC	self-interaction correction
SIE	self-interaction error
TDDFT	time-dependent density functional theory
vo	virtual-occupied
vv	virtual-virtual
XC	exchange-and-correlation
ZPL	zero phonon line

Acknowledgements

I would like to dedicate this section to the people who were vital to my PhD journey. Thank you, Hannes, for teaching me so many things over the years, not only just scientifically but also how to prioritize my scatterbrain ideas and perhaps not to tackle the very curious but not so important idea first. Thank you, Gianluca, for always having dedicated time to long discussions often about science but sometimes just about what groups of words deserve hyphens and what words are allowed to have plural forms. I now have a virtually infinite supply of hills to die on! Thank you, Elvar, for training my tenacity for what is to come in my life in long derivation sessions. I now know that a solution will always eventually appear if I only stare at a whiteboard long enough. Thank you, Philipp, for teaching me different views and scientific languages observing and expressing the same problem, enabling me to communicate more clearly. Thank you to my parents for always being there also and especially when things get tough. It is very reassuring to know that I can rely on you. Thank you, André, for motivating me to exercise regularly and to hone and develop my cooking skills with you. It has been tough to keep both activities up now that you are gone. Lastly, I would like to extend my appreciation to all of my colleagues and friends from the group and from Germany. Thank you all for all the fun events!

1 Introduction

The way to a sustainable human lifestyle is paved by renewable energy sources. Among the many forms of renewable energy, solar energy is the most intriguing in the context of chemical applications. Solar light can be thought of as an abundance of small energy units, photons, that can be absorbed by a chemical system promoting it from an equilibrium ground state to a non-equilibrium excited state with higher energy and a limited lifetime. As the system relaxes back to the ground state, the excess energy can be harnessed and stored, for instance, as electrical energy or as chemical bonds. These concepts form the basis of the field of photochemistry [1].

Photochemical devices to convert solar energy into usable forms of energy [2] face many challenges. Photovoltaic cells, for example, which convert solar energy into electrical energy [3], are bound in terms of their conversion efficiency by the Shockley-Queisser limit [4]. This theoretical efficiency limit may be broken by exciting more than one electron with a single photon, which could be achieved with singlet fission [5], which is the process of a singlet exciton splitting into two triplet excitons. The reverse process, triplet-triplet annihilation [6], where two triplet excitons combine to form a higher-energy singlet exciton, could be used to access the part of the solar spectrum with photon energy below the excitation energy of the absorbing system, providing a different approach to break the Shockley-Queisser limit. Intramolecular charge transfer plays an important role in dye-sensitized photovoltaic cells [7]. However, our understanding of these processes is currently limited.

In order to advance in these sectors, a detailed mechanistic understanding of the underlying excited state processes is required. This thesis deals with variational time-independent direct orbital optimization methods for density functional calculations of excited electronic states with which for instance these processes can be simulated.

1.1 State of the Art

In quantum-chemical calculations [8–10] of systems of bonded atoms, the Born-Oppenheimer approximation is typically applied. It factorizes the total wave function of the system into an electronic and a nuclear part. This partitioning allows one to focus on the electronic Schrödinger equation, where the explicit dependence on the nuclear degrees of freedom has been reduced to a parametric dependence. The electronic Schrödinger equation is then approximated to become solvable for the lowest-energy solution corresponding to the ground electronic state. One of the most successful approximations is Kohn-Sham density functional theory [11, 12] since it combines low computational cost with reasonable accuracy and broad applicability. Excited electronic states are higher-energy solutions to the electronic Schrödinger equation. The most commonly used density functional theory approach to calculate excited states is time-dependent density functional theory [13, 14] (TDDFT). TDDFT is a perturbative method when used within linear-response and the adiabatic approximation [15], which applies time-independent density functionals developed for ground state calculations to excited states, to make the method computationally tractable. These approximations limit the usability of TDDFT to excited states that can be described by a linear combination of single excitations with respect to the ground state and lead to deficiencies in the description of charge transfer excited states and a qualitatively incorrect description of conical intersections, degeneracies between adiabatic electronic states, between the reference state and response states [16]. Some of these challenges are addressed by recent improvements of TDDFT [17–22], but typically come at higher complexity and computational cost of the methodology. Variational time-independent techniques [23–26] provide an alternative approach analogous to ground state calculations [27–31], where excited states are found as KS solutions corresponding to stationary points higher in energy than the ground state solution [32] on the surface defined by the variation of the energy as a function of the electronic degrees of freedom.

1.2 Contributions to the Field

In this thesis, a direct optimization generalized mode following method for variational time-independent calculations of excited states is presented and its performance assessed addressing the following research questions:

1. Variational time-independent density functional calculations of excited electronic states are prone to variational collapse to lower-energy solutions than the target solution. How can convergence to the target solution be achieved without the risk of variational collpse? In consecutive calculations at different positions of the nuclei, multiple electronic solutions can emerge from one. How can these solutions be differentiated and which solutions should be chosen?

2. Perdew-Zunger self-interaction correction can generate spurious solutions on the energy surface defined by the electronic degrees of freedom. How can these spurious solutions be identified and avoided systematically?

3. Linear-response adiabatic time-dependent density functional theory yields qualitatively incorrect topologies of avoided crossings and conical intersections. Can the correct topology be obtained with direct optimization methods?

4. Linear-response adiabatic time-dependent density functional theory performs poorly on charge transfer excited electronic states of organic molecules. Can variational time-independent direct orbital optimization methods perform better?

5. The correct description of point defects in solid-state systems relevant for quantum computing applications typically requires computationally expensive high-level quantum chemistry methods. Can direct optimization methods be used in this context to give a more favorable balance of efficiency and accuracy? More specifically, can methods based on density functional theory predict the correct energetic order of the excited electronic states of the negatively charged nitrogen-vacancy defect in diamond?

All implementations used have been made in the grid-based projector augmented wave (GPAW) software [33].

2 Mean-Field Theories for Ground and Excited Electronic States

The electronic Hamiltonian of a non-relativistic system made up by electrons and nuclei given by the Born-Oppenheimer approximation in the absence of an external field is

$$\hat{\mathbf{H}}_e = \hat{\mathbf{T}} + \sum_{i=1}^{N_e} \hat{\mathbf{V}}_n(\mathbf{r}_i) + \hat{\mathbf{U}}_{ee}\,, \tag{2.1}$$

with N_e as the number of electrons and $\mathbf{r}_i$ as the degrees of freedom of electron i. Here,

$$\hat{\mathbf{T}} = -\frac{1}{2}\sum_{i=1}^{N_e} \Delta_i \tag{2.2}$$

is the kinetic energy operator, Δ_i is the Laplacian, the inner product of the nabla vector containing the derivatives with respect to all electronic degrees of freedom,

$$\hat{\mathbf{V}}_n(\mathbf{r}_i) = -\sum_{\alpha}^{N_n} \frac{Z_\alpha}{|\mathbf{r}_i - \boldsymbol{R}_\alpha|}\,, \tag{2.3}$$

with N_n as the number of nuclei, Z_α and $\boldsymbol{R}_\alpha$ as the charge and position of nucleus α, is the nuclear Coulomb potential interacting with electron i, and

$$\hat{\mathbf{U}}_{ee} = \sum_{i=1}^{N_e}\sum_{j>i}^{N_e} \frac{1}{|\mathbf{r}_i - \mathbf{r}_j|} \tag{2.4}$$

is the electron-electron Coulomb potential, and atomic units are used.

Solving

$$E_e = \langle \boldsymbol{\Psi} | \hat{\mathbf{H}}_e | \boldsymbol{\Psi} \rangle \tag{2.5}$$

for the global minimum of the electronic energy E_e yields the energy and wave function Ψ of the ground electronic state, while solving for higher-energy solutions yields the energy and wave function of excited electronic states.

In practical calculations of molecular and condensed-phase systems, eq. 2.5 needs to be approximated since the explicit dependence of the electronic Hamiltonian on the two-electron Coulomb operator makes solving the problem impossible for all but the smallest systems, even with modern computational resources. Approximate mean-field theories (MFTs) such as Hartree-Fock (HF) theory [8–10] and Kohn-Sham density functional theory (KS-DFT) [11, 12] are popular due to their favorable balance of computational cost and accuracy. MFTs approximate the full electron-electron Coulomb operator as an effective one-electron operator of the form

$$\hat{\mathbf{U}}_{\text{ee}} \approx \sum_{i=1}^{N_e} \hat{\mathbf{V}}_e^{\text{MF}}(\mathbf{r}_i) \,, \tag{2.6}$$

where $\hat{\mathbf{V}}_e^{\text{MF}}(\mathbf{r}_i)$ is the mean-field potential of all electrons interacting with electron i.

MFTs describe the electronic wave function as a single Slater determinant of orthonormal one-electron wave functions. While KS-DFT is often used as a stand-alone method, the HF method typically serves as the basis for more elaborate wave function methods [8–10] such as Møller-Plesset perturbation theory, configuration interaction, and coupled cluster theory. KS-DFT can be applied as the basis of Green function and embedding methods [34] or as a substitute of HF theory in wave function methods, but care needs to be taken then to avoid double counting of electron-electron correlation effects.

2.1 Hartree-Fock Theory

The HF [8–10] mean-field electronic potential is

$$\hat{\mathbf{V}}_e^{\text{HF}}(\mathbf{r}_i) = \sum_{j=1}^{N_e} \left(\hat{\mathbf{J}}_j - \hat{\mathbf{K}}_j\right) \,, \tag{2.7}$$

with

$$\hat{\mathbf{J}}_j = \langle \psi_j | \frac{1}{|\mathbf{r}_i - \mathbf{r}_j|} | \psi_j \rangle \tag{2.8}$$

being the HF Coulomb operator and

$$\hat{\mathbf{K}}_j | \psi_i \rangle = \langle \psi_j | \frac{1}{|\mathbf{r}_i - \mathbf{r}_j|} | \psi_i \rangle | \psi_j \rangle \tag{2.9}$$

being the HF exchange operator defined by its action on a one-electron wave function ψ_i exchanging the electronic indices of the wave function and the operator.

The resulting HF energy is

$$\begin{aligned} E_e^{\mathrm{HF}} = & \sum_i^{N_e} \left(- \langle \psi_i | \frac{1}{2} \Delta | \psi_i \rangle - \langle \psi_i | \sum_\alpha^{N_A} \frac{Z_\alpha}{|\mathbf{r} - \boldsymbol{R}_\alpha|} | \psi_i \rangle \right) \\ & + \frac{1}{2} \sum_{ij}^{N_e} \left(\langle \psi_i \psi_j | \frac{1}{|\mathbf{r} - \mathbf{r}'|} | \psi_i \psi_j \rangle - \langle \psi_i \psi_j | \frac{1}{|\mathbf{r} - \mathbf{r}'|} | \psi_j \psi_i \rangle \right) , \end{aligned} \tag{2.10}$$

where the first and second one-electron terms are the kinetic energy and electron-nuclear attraction, respectively, and the first and second two-electron terms are the electron-electron repulsion and exchange terms, respectively.

The braket notation $\langle | \, | \rangle$ indicates integration over the electronic degrees of freedom. General elements of the matrix representations of one- and two-electron operators, $\hat{O}^{1\mathrm{e}}$ and $\hat{O}^{2\mathrm{e}}$, read

$$O_{ij}^{1\mathrm{e}} = \langle \psi_i | \hat{\mathbf{O}}^{1\mathrm{e}} | \psi_j \rangle = \int d\mathrm{x} \psi_i^* (\mathrm{x}) \hat{\mathbf{O}} (\mathrm{x}) \psi_j (\mathrm{x}) \tag{2.11}$$

and

$$\begin{aligned} O_{ijkl}^{2\mathrm{e}} &= \langle \psi_i \psi_j | \hat{\mathbf{O}}^{2\mathrm{e}} | \psi_k \psi_l \rangle \\ &= \int d\mathrm{x} d\mathrm{x}' \psi_i^* (\mathrm{x}) \psi_j^* (\mathrm{x}') \hat{\mathbf{O}} (\mathrm{x}, \mathrm{x}') \psi_k (\mathrm{x}) \psi_l (\mathrm{x}') , \end{aligned} \tag{2.12}$$

respectively, where x convolutes the spatial and spin coordinates of the electrons.

2.2 Kohn-Sham Density Functional Theory

The main idea of KS-DFT is to improve upon the HF MFT by replacing the HF exchange operator by a functional of the electron density describing both electron-electron exchange and electron-electron Coulomb correlation, the latter of which is by definition missing in HF theory. Density functional theory (DFT) is an exact theory (within the Born-Oppenheimer approximation) based on the Hohenberg-Kohn (HK) theorems. Approximations to DFT are in practice made in the exchange-and-correlation (XC) functional.

2.2.1 Hohenberg-Kohn Theorems and Universal Density Functional

The HK theorems [11] provide the foundation of DFT. The first HK theorem establishes a unique link between the electron density

$$\rho(\mathbf{r}) = N_e \int \Psi^*(\mathbf{r}_1, ..., \mathbf{r}_{N_e}) \Psi(\mathbf{r}_1, ..., \mathbf{r}_{N_e}) \prod_{i=2}^{N_e} d\mathbf{r}_i \tag{2.13}$$

and an external potential, $v(\mathbf{r})$, making the electronic energy a unique functional of the electron density as

$$E_e[\rho] = \int d\mathbf{r} v(\mathbf{r}) \rho(\mathbf{r}) + F[\rho] , \tag{2.14}$$

where $F[\rho]$ is the universal HK functional, which can further be separated into the Coulomb energy and another universal functional, $G[\rho]$

$$F[\rho] = \frac{1}{2} \int d\mathbf{r} d\mathbf{r}' \frac{\rho(\mathbf{r}) \rho(\mathbf{r}')}{|\mathbf{r} - \mathbf{r}'|} + G[\rho] . \tag{2.15}$$

Similarly to eq. 2.5, solving eq. 2.14 for a minimum of the electronic energy yields the ground electronic energy, but the minimization is performed with respect to ρ and does not rely on orbitals. This minimum energy principle is established in the second HK theorem.

2.2.2 Kohn-Sham Formalism

The Kohn-Sham (KS) formalism [12] introduces a system of non-interacting electrons with the same electron density as the interacting electrons, which allows for the universal functional $G[\rho]$ to be written as

$$G[\rho] = T_s[\rho] + E_{\mathrm{XC}}[\rho] \,, \tag{2.16}$$

with T_s as the kinetic energy of the non-interacting system and $E_{\mathrm{XC}}[\rho]$ as the XC functional. Substituting eq. 2.16 in eq. 2.15 and the result in eq. 2.14, one obtains an expression for the electronic energy

$$E_e[\rho] = T_s[\rho] + \int d\mathbf{r} v(\mathbf{r}) \rho(\mathbf{r}) + \frac{1}{2} \int d\mathbf{r} d\mathbf{r}' \frac{\rho(\mathbf{r}) \rho(\mathbf{r}')}{|\mathbf{r} - \mathbf{r}'|} + E_{\mathrm{XC}}[\rho] \,. \tag{2.17}$$

The stationary condition is found by taking the derivative of eq. 2.17 with respect to ρ as

$$\frac{\partial T_s[\rho]}{\partial \rho} + v(\mathbf{r}) + v_{\mathrm{U}}(\mathbf{r}) + v_{\mathrm{XC}}(\mathbf{r}) \stackrel{!}{=} 0 \,, \tag{2.18}$$

where $v(\mathbf{r})$, $v_{\mathrm{U}}(\mathbf{r})$, and $v_{\mathrm{XC}}(\mathbf{r})$ are the external, Coulomb, and XC potentials, respectively. The stationary condition of the non-interacting system is

$$\frac{\partial T_s[\rho]}{\partial \rho} + v_s(\mathbf{r}) \stackrel{!}{=} 0 \,, \tag{2.19}$$

where the non-interacting external potential, $v_s(\mathbf{r})$, is chosen such that the solutions to eqs.2.18 and 2.19 coincide as

$$v_s(\mathbf{r}) = v(\mathbf{r}) + v_{\mathrm{U}}(\mathbf{r}) + v_{\mathrm{XC}}(\mathbf{r}) \,. \tag{2.20}$$

Introducing orbitals, one obtains the set of self-consistent equations

$$\left(-\frac{1}{2}\Delta_i + v(\mathbf{r}_i) + v_{\mathrm{U}}(\mathbf{r}_i) + v_{\mathrm{XC}}(\mathbf{r}_i) \right) |\psi_i\rangle = \varepsilon_i |\psi_i\rangle \tag{2.21}$$

for the non-interacting system. The kinetic energy and the electron density in the KS formalism are

$$T_s = -\frac{1}{2} \sum_{i=1}^{N_e} \langle \psi_i | \Delta_i | \psi_i \rangle \tag{2.22}$$

and

$$\rho = \sum_{i=1}^{N_e} |\psi_i|^2 \,, \tag{2.23}$$

respectively.

The final expression for the KS energy

$$\begin{aligned} E_e^{\mathrm{KS}} = \sum_{i}^{N_e} \left(-\langle \psi_i | \frac{1}{2} \Delta | \psi_i \rangle - \langle \psi_i | \sum_{\alpha}^{N_A} \frac{Z_\alpha}{|\mathbf{r} - \boldsymbol{R}_\alpha|} | \psi_i \rangle \right) \\ + \frac{1}{2} \sum_{ij}^{N_e} \left(\langle \psi_i \psi_j | \frac{1}{|\mathbf{r} - \mathbf{r}'|} | \psi_i \psi_j \rangle - E_{\mathrm{XC}}(\rho) \right) \,, \end{aligned} \tag{2.24}$$

is similar to eq. 2.10 for the HF energy with the HF exchange replaced by the XC functional.

2.2.3 Types of Approximate Exchange-and-Correlation Functionals

Approximate XC functionals are divided into groups depending on the order of the derivative of the electron density they depend on. The local density approximation (LDA) [35] depends only on the direct local value of the density. The generalized gradient approximation (GGA) introduces dependence on the gradient of the density, and the meta GGA adds dependence on the Laplacian of the density or kinetic energy density.

The KS formalism can be generalized to use any type of effective non-interacting system such as an HF system. This generalized KS scheme [36] forms the basis for hybrid XC functionals, which describe part of the exchange interaction with HF exchange and the remainder with an XC functional of the density. Double-hybrid XC functionals additionally perform a perturbative calculation with the KS-DFT orbitals.

Generally, higher computational effort and higher accuracy can be expected of XC functionals in the order LDA, GGA, meta GGA, hybrid functionals, double-hybrid approach, but this ordering is not strict, and indeed, even the LDA may in certain cases outperform double-hybrid functionals in both accuracy and certainly in efficiency.

2.2.4 Perdew-Zunger Self-Interaction Correction

The sums over the two-electron terms in eqs. 2.10 and 2.24 explicitly include terms with $i = j$. These terms

$$U_{iiii} = \langle \psi_i \psi_i | \frac{1}{|\mathbf{r} - \mathbf{r}'|} | \psi_i \psi_i \rangle \tag{2.25}$$

represent the Coulomb interaction of electron i with itself and are commonly referred to as Hartree self-interaction terms. Since these spurious self-interaction terms occur both in the electron-electron Coulomb repulsion as well as the exchange interaction in HF theory, they cancel exactly leaving the HF energy self-interaction free. Due to the approximate nature of the XC functional in KS-DFT, the Hartree self-interaction terms are not exactly canceled by exchange self-interaction terms anymore (unless a correction is incorporated into the XC functional) introducing the infamous self-interaction error (SIE) into KS-DFT.

Perdew and Zunger propose a one-electron self-interaction correction (SIC) [37] according to

$$E_e^{\mathrm{SIC}}(\rho_1, ..., \rho_{N_e}) = E_e^{\mathrm{KS}} - \sum_{i=1}^{N_e} \left(U_{iiii} + E_{\mathrm{XC}}(\rho_i) \right) . \tag{2.26}$$

While the KS energy depends only on the total electron density, which is invariant to unitary transformations among equally occupied orbitals, and is therefore invariant to such unitary transformations as well, the dependence of the SIC energy on each orbital density

$$\rho_i = |\psi_i|^2 \tag{2.27}$$

causes it to vary with unitary transformations among the occupied orbitals. Since the SIE is a many-body effect, this one-electron SIC is only exact for systems with a single electron.

3 Variational Orbital Optimization Methods

3.1 Molecular Orbitals and Bands

There are three common kinds of ansatz for the single-electron wave functions. The molecular orbitals (MOs) of molecular systems are often described using a linear combination of atomic orbitals (LCAO), while the bands in solid-state systems typically employ a finite difference (FD) or plane wave (PW) ansatz. Any of these formalisms can, however, be applied in any context, and it can, in particular, be advantageous to use FD or PW schemes for molecular systems since they provide a more systematic way to reach the basis set limit. In the following, the term MO is used for the one-electron wave functions in both molecular and solid-state systems.

3.1.1 Linear Combination of Atomic Orbitals

The most common ansatz for the MOs in calculations of molecular systems is the LCAO. In the LCAO method, a linear expansion in a set of M basis functions $\boldsymbol{\phi} = (|\phi_1\rangle, ..., |\phi_M\rangle)$ is performed yielding M MOs $\boldsymbol{\psi} = (|\psi_1\rangle, ..., |\psi_M\rangle)$ as

$$\boldsymbol{\psi} = \boldsymbol{\phi}\mathbf{C} \tag{3.1}$$

with $\mathbf{C}$ being an $M \times M$ matrix of expansion coefficients. Orthonormality constraints are applied to the MOs *via* the coefficient matrix but not necessarily to the basis functions. The angular part of the basis functions is represented by spherical harmonics, while the radial part is often chosen to fit atomic orbitals usually using (contracted) Gaussian functions or direct numerical atomic orbitals. The advantage of an LCAO basis set is the relatively good accuracy that can be achieved with a modest amount of functions. However, achieving very high accuracy with an LCAO

basis set may prove difficult, as these basis sets can become overcomplete when many basis functions are employed leading to small eigenvalues of the basis function overlap matrix causing numerical problems in practical calculations.

3.1.2 Finite Difference and Plane Waves

In the FD ansatz, the MOs are expanded in a series of delta functions localized at grid points on a three-dimensional real space grid. The number of grid points and their locations in real space are determined by the size of the real space grid and the spacing between the grid points. The grid is typically chosen to be uniform, but the grid spacing can be adapted such that the regions around the nuclei have a denser grid than those far away from the nuclei to account for the oscillations of the wave functions around the nuclei.

In the PW ansatz, the MOs are expanded in a set of PWs in reciprocal space. The advantage of this type of reciprocal space ansatz is the computational efficiency as compared to the FD ansatz since properties can be evaluated using efficient fast Fourier transformation algorithms.

Both the FD and the PW ansatz follow the idea of quantity over quality of the basis functions. In this way, the basis set limit can be approached systematically by changing only a small set of parameters, the grid spacing and size in FD calculations and the grid spacing and size and the cutoff energy of the PWs in PW calculations.

3.2 Direct Optimization Technique

Direct optimization (DO) methods [23–31] aim to find the unitary matrix, $\mathbf{U}_{\text{stat}}$, that transforms the set of initial MOs, $\mathbf{\Psi}_0$, into the set of MOs, $\mathbf{\Psi}_{\text{stat}}$, that makes the energy stationary

$$\mathbf{\Psi}_{\text{stat}} = \mathbf{U}_{\text{stat}} \mathbf{\Psi}_0 \,. \tag{3.2}$$

A unitary matrix can conveniently be expressed as the exponential

$$\mathbf{U} = e^{\boldsymbol{\kappa}} \,, \tag{3.3}$$

of an anti-Hermitian matrix $\boldsymbol{\kappa}$ containing pair-wise orbital rotations. Since the exponential is a monotonic function, the search for a stationary point in the space of unitary matrices can be recast as a search for a stationary point in the space of matrices $\boldsymbol{\kappa}$ as

$$E_e^{\text{stat}} = \underset{\mathbf{U}}{\text{stat}} \left(\mathbf{U}\boldsymbol{\Psi}_0\right) = \underset{\boldsymbol{\kappa}}{\text{stat}} \left(e^{\boldsymbol{\kappa}}\boldsymbol{\Psi}_0\right) . \tag{3.4}$$

3.3 Orbital Rotations and Energy Derivatives

The orbital rotation matrix $\boldsymbol{\kappa}$ can be separated into the blocks

$$\boldsymbol{\kappa} = \begin{pmatrix} \boldsymbol{\kappa}_{\text{oo}} & \boldsymbol{\kappa}_{\text{ov}} \\ \boldsymbol{\kappa}_{\text{vo}} & \boldsymbol{\kappa}_{\text{vv}} \end{pmatrix} . \tag{3.5}$$

The occupied-occupied (oo), occupied-virtual (ov), virtual-occupied (vo), and virtual-virtual (vv) blocks of $\boldsymbol{\kappa}$, $\boldsymbol{\kappa}_{\text{oo}}$, $\boldsymbol{\kappa}_{\text{ov}}$, $\boldsymbol{\kappa}_{\text{vo}}$, and $\boldsymbol{\kappa}_{\text{vv}}$, mix pairs of occupied and occupied orbitals, occupied and virtual, virtual and occupied, and virtual and virtual orbitals, respectively. The orthonormality constraints between the MOs are satisfied by requiring the orbital rotation matrix to be anti-Hermitian

$$\boldsymbol{\kappa} = -\boldsymbol{\kappa}^{\dagger} , \tag{3.6}$$

provided the initial MOs are orthonormal. In this way, $\boldsymbol{\kappa}_{\text{vo}}$ is eliminated as a degree of freedom of the energy since

$$\boldsymbol{\kappa}_{\text{vo}} = -\boldsymbol{\kappa}_{\text{ov}}^{\dagger} . \tag{3.7}$$

The gradient of the KS energy, eq. 2.24, with respect to the elements of $\boldsymbol{\kappa}$ is the gradient of the exponential map [31]

$$\frac{\partial E_e^{\text{KS}}}{\partial \kappa_{ij}} = \frac{2-\delta_{ij}}{2} \left[\int_0^1 dt e^{t\boldsymbol{\kappa}} \mathbf{L} e^{-t\boldsymbol{\kappa}} \right]_{ji} , \tag{3.8}$$

where δ_{ij} is an element of the identity matrix and $\mathbf{L}$ is the Lagrangian matrix with elements

$$L_{ij} = \left(f_i - f_j\right) H_{ij}^{\text{KS}} , \tag{3.9}$$

with f_i as the occupation numbers of the MOs and

$$H_{ij}^{\mathrm{KS}} = \langle \psi_i | \, \hat{\mathbf{H}}_e^{\mathrm{KS}} \, | \psi_j \rangle \tag{3.10}$$

as the matrix elements in the basis of MOs of the KS Hamitonian

$$\hat{\mathbf{H}}_e^{\mathrm{KS}} = -\frac{1}{2}\Delta + v(\mathbf{r}) + v_{\mathrm{U}}(\mathbf{r}) + v_{\mathrm{XC}}(\mathbf{r}) \, . \tag{3.11}$$

As the anti-Hermitian matrices form the Lie-algebra corresponding to the Lie-group of their exponentials, the integral in eq. 3.8 can be expressed in the commutator series [38–41]

$$\int_0^1 dt e^{t\boldsymbol{\kappa}} \mathbf{L} e^{-t\boldsymbol{\kappa}} = \mathbf{L} + \frac{1}{2!}[\boldsymbol{\kappa}, \mathbf{L}] + \frac{1}{3!}[\boldsymbol{\kappa}, [\boldsymbol{\kappa}, \mathbf{L}]] + \ldots \tag{3.12}$$

which can be truncated if the elements of $\boldsymbol{\kappa}$ are sufficiently small, which is ensured if the unitary transformation is applied to the orbitals at every step, resetting the elements of $\boldsymbol{\kappa}$ to zero.

Since the KS energy is invariant to unitary transformations among equally occupied orbitals, which follows from eq. 3.9, $\boldsymbol{\kappa}_{\mathrm{oo}}$ and $\boldsymbol{\kappa}_{\mathrm{vv}}$ are not degrees of freedom of the KS energy, so the orbital rotation matrix can be parameterized as

$$\boldsymbol{\kappa}_{\mathrm{KS}} = \begin{pmatrix} \mathbf{0} & \boldsymbol{\kappa}_{\mathrm{ov}} \\ -\boldsymbol{\kappa}_{\mathrm{ov}}^{\dagger} & \mathbf{0} \end{pmatrix} , \tag{3.13}$$

where $\mathbf{0}$ denotes the null matrix.

The elements of the HF electronic Hessian matrix containing the second derivatives of the energy with respect to the electronic degrees of freedom in a spin-restricted formalism are [42]

$$\mathscr{H}_{\kappa_{ij}\kappa_{kl}} = \delta_{ik}\delta_{jl}\left(\varepsilon_i - \varepsilon_j\right) + 4U_{ikjl} - U_{ijkl} - U_{ijlk} \, , \tag{3.14}$$

where

$$U_{ijkl} = \langle \psi_i \psi_j | \, \frac{1}{|\mathbf{r} - \mathbf{r}'|} \, | \psi_k \psi_l \rangle \tag{3.15}$$

are the elements of the matrix representation of the Coulomb operator. The evaluation of the electronic Hessian matrix thus involves the calculation of the orbital energies and the matrix representation of the Coulomb operator in the occupied orbital space, which is a computationally expensive endeavor. Equation 3.14 inspires the approximate diagonal Hessian

$$\mathscr{H}^0_{\kappa_{ij}\kappa_{ij}} = \left(f_i - f_j\right)\left(\varepsilon_j - \varepsilon_i\right) . \tag{3.16}$$

If SIC is used, the Lagrangian in eq. 3.9 changes to [25]

$$L_{ij} = \left(f_i - f_j\right) H^{\mathrm{KS}}_{ij} - f_i V^{\mathrm{SIC}}_{ij} + f_j V^{\mathrm{SIC}*}_{ji} , \tag{3.17}$$

with the elements of the SIC potential matrix $\mathbf{V}^{\mathrm{SIC}}$ being

$$V^{\mathrm{SIC}}_{ij} = \langle \psi_i(\mathbf{r}) | \left(\int d\mathbf{r}' \frac{n_i(\mathbf{r}')}{|\mathbf{r} - \mathbf{r}'|} + v_{\mathrm{XC}}\left[n_i(\mathbf{r})\right] \right) | \psi_j \rangle . \tag{3.18}$$

Since the SIC terms in eq. 3.17 scale directly with the occupation numbers, as opposed to the occupation number differences, these terms are finite for the orbital rotations in $\boldsymbol{\kappa}_{\mathrm{oo}}$. Consequently, the SIC introduces additional degrees of freedom of the energy and the orbital rotation matrix becomes

$$\boldsymbol{\kappa}_{\mathrm{SIC}} = \begin{pmatrix} \boldsymbol{\kappa}_{\mathrm{oo}} & \boldsymbol{\kappa}_{\mathrm{ov}} \\ -\boldsymbol{\kappa}^{\dagger}_{\mathrm{ov}} & \mathbf{0} \end{pmatrix} . \tag{3.19}$$

Due to the variational nature of DO, immediate access to atomic forces in ground and excited electronic states is given by the Hellman-Feynman theorem.

3.4 Evaluation of the Matrix Exponential

The matrix exponential in eq. 3.3 needs to be evaluated at every electronic DO step, so it is wise to consider the algorithm used. Even though ref. 43 reviews an astounding 19 more or less "dubious" ways of evaluating the exponential of a matrix, only the two least dubious ways, eigendecomposition, and the scaling and squaring Padé approximation are considered in the following.

3.4.1 Eigendecomposition

Eigendecomposition can be used to evaluate the matrix exponential as

$$e^{\boldsymbol{\kappa}} = \mathbf{W} e^{-i\boldsymbol{\Lambda}} \mathbf{W}^{\dagger}, \tag{3.20}$$

where $\boldsymbol{\Lambda}$ and $\mathbf{W}$ are the real-valued diagonal matrix of eigenvalues and the column matrix of eigenvectors of $i\boldsymbol{\kappa}$, respectively. Since this algorithm involves the diagonalization of a large matrix, it is computationally rather expensive.

3.4.2 Padé Approximation

The (p,q) Padé approximation to the matrix exponential is

$$e^{\boldsymbol{\kappa}} \approx \frac{P_{pq}(\boldsymbol{\kappa})}{Q_{pq}(\boldsymbol{\kappa})}, \tag{3.21}$$

with

$$P_{pq}(\boldsymbol{\kappa}) = \sum_{i=0}^{p} \frac{(p+q-i)!\,p!}{(p+q)!\,i!\,(p-i)!} \boldsymbol{\kappa}^i \tag{3.22}$$

and

$$Q_{pq}(\boldsymbol{\kappa}) = \sum_{i=0}^{q} \frac{(p+q-i)!\,q!}{(p+q)!\,i!\,(q-i)!} (-\boldsymbol{\kappa})^i . \tag{3.23}$$

The Padé approximation fails if $Q_{pq}(\boldsymbol{\kappa})$ is singular, but according to ref. 43 it is guaranteed to be non-singular if p and q are chosen to be large enough. Diagonal Padé approximants ($p = q$) are preferred over off-diagonal ones since the order of diagonal approximants is $2p$ and therefore larger than the order of $p+q$ for off-diagonal approximants, while the computational effort is identical.

3.4.3 Scaling and Squaring

If the norm of $\boldsymbol{\kappa}$ is small ($||\boldsymbol{\kappa}|| << 1$), the Padé approximation can be applied with small values for p and q, increasing the efficiency of the evaluation of the matrix exponential. The idea behind the scaling and

squaring approach [44] is to make use of the fundamental property of the exponential function

$$e^{\boldsymbol{\kappa}} = \left(e^{\frac{\boldsymbol{\kappa}}{m}}\right)^m \tag{3.24}$$

in order to apply the Padé approximation to the exponential of a scaled matrix by dividing $\boldsymbol{\kappa}$ by 2 as often as needed to ensure a small enough norm and squaring the result accordingly to obtain the matrix exponential. The optimal combination of p for the diagonal Padé approximant and j for $m = 2^j$ in eq. 3.24 can be chosen automatically [43, 44] to provide maximum efficiency.

3.5 Electronic Energy Surface

A model two-dimensional electronic energy surface of the hydrogen molecule at a distance of 2.387 Å between the atoms obtained using a minimum basis set of numerical 1s orbitals [45, 46] and the PBE [47, 48] functional with a spin-unrestricted formalism is shown in fig. 3.1. The electronic degrees of freedom are the orbital rotations ϕ_α and ϕ_β mixing the two orbitals in the α and β spin channels, respectively, according to

$$\begin{pmatrix} \psi_\alpha^1 \\ \psi_\alpha^0 \\ \psi_\beta^1 \\ \psi_\beta^0 \end{pmatrix} = \begin{pmatrix} \cos\phi_\alpha & \sin\phi_\alpha & 0 & 0 \\ -\sin\phi_\alpha & \cos\phi_\alpha & 0 & 0 \\ 0 & 0 & \cos\phi_\beta & \sin\phi_\beta \\ 0 & 0 & -\sin\phi_\beta & \cos\phi_\beta \end{pmatrix} \begin{pmatrix} \sigma_g(R) \\ \sigma_u^*(R) \\ \sigma_g(R) \\ \sigma_u^*(R) \end{pmatrix}, \tag{3.25}$$

where $\sigma_g = \frac{1}{\sqrt{2}}(1s_A + 1s_B)$ and $\sigma_u^* = \frac{1}{\sqrt{2}}(1s_A + 1s_B)$ are the bonding and antibonding σ orbitals, respectively, of the hydrogen molecule in the ground state chosen as the reference orbitals of the orbital rotations and $1s_A$ and $1s_B$ are $1s$ atomic orbitals centered at hydrogen atoms A and B, respectively. The superscripts 1 and 0 indicate occupied and virtual orbitals, respectively. The idea behind the DO approach defined by eq. 3.4 is to find the stationary points on this energy surface. The global minimum corresponds to the ground electronic state, while higher-energy stationary points correspond to excited states [32]. In order to target a specific excited state, a ground state solution at a given geometry is obtained first, an excitation is performed generating a non-aufbau configuration of the ground state MOs and a saddle point search is initialized.

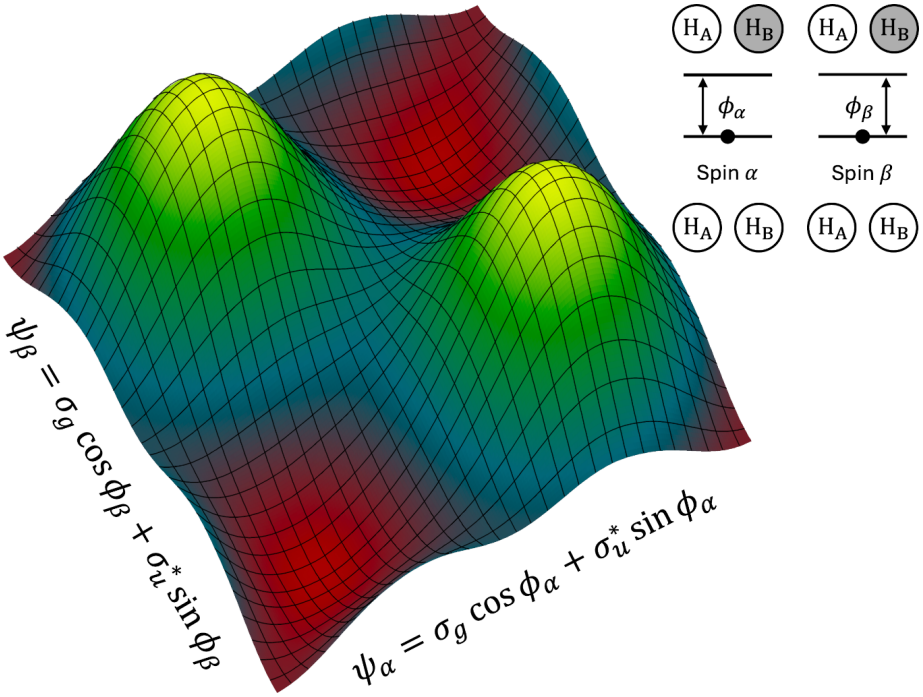

Figure 3.1. Electronic energy surface of the hydrogen molecule at a distance of 2.387 Å between the atoms obtained using a minimum basis set of numerical 1s orbitals and the PBE functional with a spin-unrestricted formalism. The inset shows a schematic of the electronic degrees of freedom which are the orbital rotations ϕ_α and ϕ_β mixing the orbitals in the α and β spin channels, respectively. The reference orbitals of the orbital rotations are the bonding σ_g orbital for the occupied orbital and the antibonding σ_u^* orbital for the virtual orbital in both spin channels.

3.6 Quasi-Newton Methods

Due to their efficiency, quasi-Newton (QN) methods [49] are the linear optimization methods of choice for the DO method. QN methods are approximations to Newton's method which applies a quadratic model to the objective function, f, to evaluate the search direction

$$\boldsymbol{p}_k^{\mathrm{N}} = -\nabla^{-2} f_k \nabla f_k \tag{3.26}$$

of each optimization step, k. In the orbital optimization case with KS-DFT, the objective function is the KS energy given by eq. 2.24. The Hessian matrix, $\nabla^2 f$ contains all second derivatives of the objective function. Even though the Hessian matrix is symmetric, evaluating and inverting it at every optimization step, as suggested by eq. 3.26, is infeasible in the context of electronic structure calculations. Limited-memory [50] QN methods, instead, store information of the previous m optimization steps in form of scalars and vectors to form an approximate inverse Hessian, $\mathbf{B}_k$, giving the step

$$\boldsymbol{p}_k^{\mathrm{QN}} = -\mathbf{B}_k \nabla f_k \,. \tag{3.27}$$

The limited-memory Broyden-Fletcher-Goldfard-Shanno (L-BFGS) [51] QN method is taylored toward minimizations and can therefore be applied to ground state calculations. Excited state calculations require QN methods that can form an indefinite model inverse Hessian and thus converge to saddle points. Suitable QN inverse Hessian update methods include the limited-memory symmetric rank-1 (L-SR1) [24, 52], limited-memory Powell (L-P) [53], and limited-memory Bofill (L-B) [54] methods.

3.6.1 Limited-Memory Broyden-Fletcher-Goldfarb-Shanno Method

In the L-BFGS method, the inverse Hessian, $\mathbf{B}$, is updated at every optimization step k by

$$\begin{aligned}\mathbf{B}_{k+1}^{\mathrm{L-BFGS}} = \mathbf{V}_k^T \Bigg[\prod_{a=k-1}^{k-m} \left(\mathbf{V}_a^T\right) \mathbf{B}_k^0 \prod_{b=k-m}^{k-1} \left(\mathbf{V}_b\right) \\ + \mathbf{V}_k^T \sum_{i=k-m}^{k-1} \theta_i \prod_{a=k-1}^{i+1} \left(\mathbf{V}_a^T\right) \boldsymbol{s}_i \boldsymbol{s}_i^T \prod_{b=i+1}^{k-1} \left(\mathbf{V}_b\right) \Bigg] \mathbf{V}_k + \theta_k \boldsymbol{s}_k \boldsymbol{s}_k^T \,,\end{aligned} \tag{3.28}$$

where

$$\mathbf{V}_k = \mathbf{I} - \theta_k \boldsymbol{y}_k \boldsymbol{s}_k^T \,, \tag{3.29}$$

with $\mathbf{I}$ as the identity matrix. $\mathbf{B}_k^0$ is the inverse of an approximate Hessian, which in the case of HF and KS-DFT calculations is commonly given by eq. 3.16,

$$\theta_k = \frac{1}{\boldsymbol{y}_k^T \boldsymbol{s}_k} \,, \tag{3.30}$$

$$\boldsymbol{y}_k = \nabla f_{k+1} - \nabla f_k \,, \tag{3.31}$$

and

$$\boldsymbol{s}_k = \overrightarrow{\boldsymbol{\kappa}}_{k+1} - \overrightarrow{\boldsymbol{\kappa}}_k \,, \tag{3.32}$$

with $\overrightarrow{\boldsymbol{\kappa}}$ as the vector containing the elements of $\boldsymbol{\kappa}$. The inverse Hessian is never explicitly evaluated, but instead, eq. 3.28 is directly applied to its matrix vector products. In the case of L-BFGS, only the search direction in eq. 3.27 needs to be updated at every optimization step and the previous vectors $\boldsymbol{s}$ and $\boldsymbol{y}$ need to be stored.

3.6.2 Limited-Memory Symmetric Rank-1 Method

The L-SR1 update of the inverse Hessian applied to a vector $\boldsymbol{v}$ is [24, 52]

$$\left[\mathbf{B}^{\mathrm{L-SR1}} \boldsymbol{v}\right]_{k+1} = \mathbf{B}_k^0 \boldsymbol{v}_{k+1} + \sum_{i=k-m+1}^{k} \frac{\boldsymbol{j}_i \boldsymbol{j}_i^T}{\boldsymbol{j}_i^T \boldsymbol{y}_i} \boldsymbol{v}_{k+1} \,, \tag{3.33}$$

with

$$\boldsymbol{j}_k = \boldsymbol{s}_k - \mathbf{B}_k^{\mathrm{L-SR1}} \boldsymbol{y}_k \,, \tag{3.34}$$

implying an update of $\mathbf{B}_k^{\mathrm{L-SR1}} \boldsymbol{y}_k$ before the search direction in eq. 3.27 can be updated at every optimization step. Only the previous vectors $\boldsymbol{j}$ needs to be stored, while the dependence on $\boldsymbol{s}$ can be reduced to the inner product scalars $\boldsymbol{j}^T \boldsymbol{y}$.

3.6.3 Limited-Memory Powell Method

In the L-P method, the matrix vector product of the inverse Hessian and a vector $\boldsymbol{v}$ is

$$\left[\mathbf{B}^{\mathrm{L-P}}\boldsymbol{v}\right]_{k+1} = \mathbf{B}_k^0 \boldsymbol{v}_{k+1} \tag{3.35}$$

$$+ \sum_{i=k-m+1}^{k} \left[\boldsymbol{j}_i \boldsymbol{u}_i^T \boldsymbol{v}_{k+1} + \boldsymbol{u}_i \left(\boldsymbol{j}_i^T \boldsymbol{v}_{k+1} - \boldsymbol{y}_i^T \boldsymbol{j}_i \boldsymbol{u}_i^T \boldsymbol{v}_{k+1}\right)\right], \tag{3.36}$$

where

$$\boldsymbol{u}_k = \frac{\boldsymbol{y}_k}{\boldsymbol{y}_k^T \boldsymbol{y}_k}. \tag{3.37}$$

Similarly to the L-SR1 method, two update loops need to be performed at every optimization step. The previous vectors $\boldsymbol{u}$ need to be stored in addition to the previous vectors $\boldsymbol{j}$ and the inner product scalars $\boldsymbol{j}^T\boldsymbol{y}$.

3.6.4 Limited-Memory Bofill Method

The L-B method is a combination of the L-SR1 and L-P inverse Hessian updates defined as

$$\mathbf{B}_{k+1}^{\mathrm{L-B}} = (1-\phi_k)\,\mathbf{B}_{k+1}^{\mathrm{L-SR1}} + \phi_k \mathbf{B}_{k+1}^{\mathrm{L-P}}, \tag{3.38}$$

where

$$\phi_k = 1 - \frac{\left(\boldsymbol{y}_k^T \boldsymbol{j}_k\right)^2}{\boldsymbol{y}_k^T \boldsymbol{y}_k \boldsymbol{j}_k^T \boldsymbol{j}_k} \tag{3.39}$$

is the Bofill factor, which increases the percentage of the L-P update as the optimization gets closer to convergence. The idea behind this approach is using the fast but supposedly less robust L-SR1 method to get into the vicinity of a stationary point and gradually switch to the supposedly more robust but less efficient L-P method for the final optimization steps. In our experience however, the bare L-SR1 method typically outperforms both the L-P and L-B methods in density functional orbital optimized calculations of excited states.

3.7 Maximum Overlap Method

Time-independent density functional calculations of excited states are prone to variational collapse to solutions lower in energy than the target excited state solution. The maximum overlap method [55, 56] (MOM) is an appealing method to counteract variational collapse due to its negligible computational cost. In this approach, the occupied orbitals at each optimization step are chosen as those with the largest similarity to a set of reference orbitals, ψ_j^{ref}. The weights, ω_i, measuring the similarity between the current orbitals and the reference orbitals are typically evaluated using the absolute overlaps between the orbitals

$$\omega_i = \max_j \left(\left| O_{ij} \right| \right) \tag{3.40}$$

or the projections

$$\omega_i = \left(\sum_{j=1}^{N_e} \left| O_{ij} \right|^2 \right)^{0.5} , \tag{3.41}$$

with the overlap matrix

$$O_{ij} = \langle \psi_i | \psi_j^{\text{ref}} \rangle \, . \tag{3.42}$$

The reference orbitals are usually chosen either as the orbitals of the initial guess [55] or as the orbitals of the previous step [56].

3.8 Considerations for Consecutive Calculations

In consecutive electronic structure calculations, such as geometry optimizations, molecular dynamics simulations, and computations of potential energy curves, information about the wave function at nearby points in nuclear coordinate space is available both in computations of the ground and excited electronic states. This information may be used to improve the initial guess of DO methods and accelerate convergence of the optimization in particular for excited states since the ground state solution does not need to be evaluated beyond the first point in the sequence

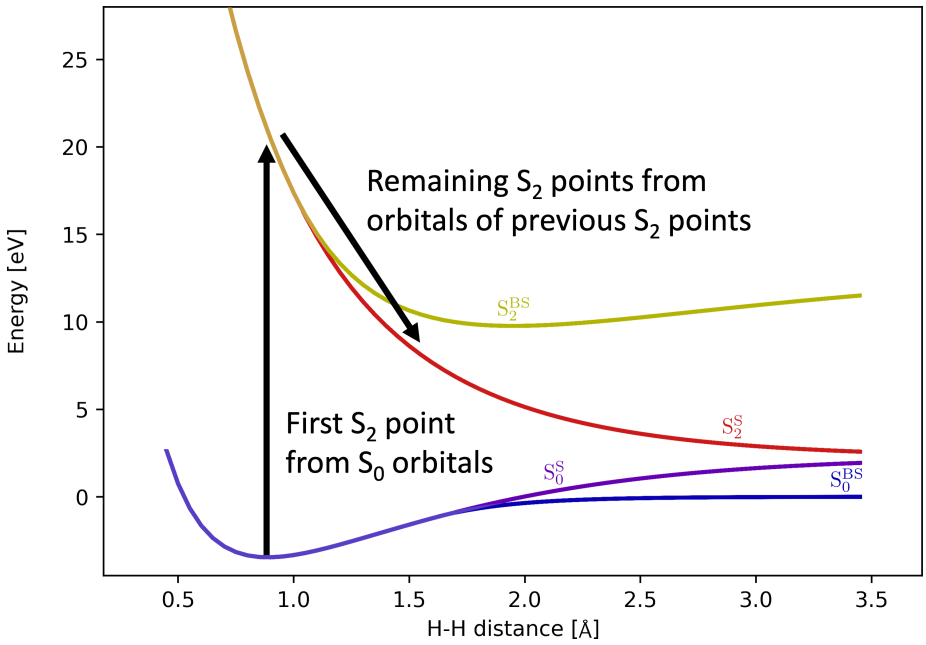

Figure 3.2. Potential energy curves of the ground and doubly excited electronic states of the hydrogen molecule model system (see sec. 3.5) illustrating the concept and challenges of consecutive electronic structure calculations at different nuclear geometries. Each potential energy curve splits into multiple curves as the distance between the hydrogen atoms is increased, with one curve, S_0^S and S_2^S, conserving the symmetries of the Hamiltonian and one curve, S_0^{BS} and S_2^{BS}, breaking the spin and spatial symmetries of the Hamiltonian, respectively. The arrows indicate the initial guess procedure for the excited state calculations. The first point in the sequence (ground state minimum geometry) is initialized with the MOs of the ground state solution with non-aufbau occupation numbers. Subsequent calculations are initialized from the MOs of the excited state solution that is closest in nuclear coordinate space.

if one is solely interested in the excited state solutions. This concept and its caveats are illustrated in fig. 3.2 for the doubly excited state of the hydrogen molecule model discussed in sec. 3.5. The energy curves of the ground state as a function of the distance between the hydrogen atoms are shown as well. In both curves, there is a point at which multiple solutions emerge from one as the distance between the atoms is increased. Solutions that conserve the symmetries of the Hamiltonian, S_0^S and S_2^S, exist at all distances. The S_0^{BS} and S_2^{BS} solutions break the spin and spatial symmetries of the Hamiltonian, respectively. The spin-mixed open-shell singly excited state and triplet solutions are not shown. While the symmetry-conserving energy curves are monotonic and become degenerate in the dissociation limit, the symmetry-broken solutions show the expected energy in this limit, with the S_0^{BS} energy curve approaching 0 and the S_2^{BS} energy curve displaying a minimum. This minimum is due to electrostatic interaction since these solutions have ionic character.

Suppose the excited state energy curve shall be evaluated starting from the minimum in the ground state energy curve. Following the arrows in fig. 3.2, the saddle point search at the first point is initialized from the ground state wave function by changing the occupation numbers to a non-aufbau configuration reflecting the character of the target excited state, which in this case correspond to an excitation from the highest occupied molecular orbital (HOMO) to the lowest unoccupied molecular orbital (LUMO) in both spin channels. Subsequent excited state saddle point searches are initialized from the wave function of the converged excited state solution at the previous geometry. Since the solutions are symmetry-conserving in the region where only one electronic solution exists, the initial guess for the first electronic structure calculation when the symmetry-broken electronic solutions become available lacks a component that breaks the symmetry and thus the symmetry-conserving energy curve is obtained systematically. The only way to obtain the symmetry-broken energy curve is to adjust the initial guess manually. The generalized mode following (GMF) method presented in sec. 3.9 provides a systematic way to converge to the symmetry-broken excited state solutions as soon as they become available.

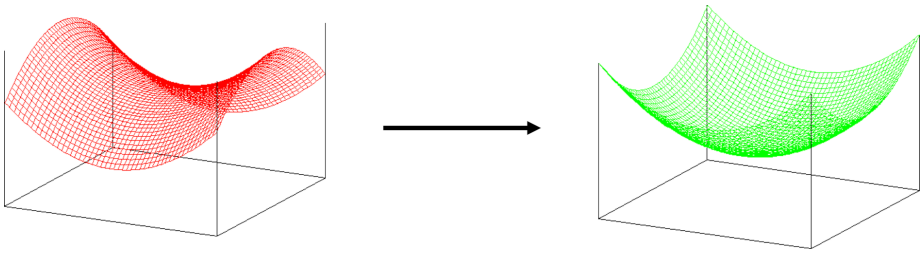

Figure 3.3. Schematic illustration of the MMF method. The objective is to find the first-order saddle point of the objective function (red). A modified gradient is evaluated by inverting the projection of the total gradient on the eigenvector corresponding to the lowest eigenvalue of the Hessian. This modified gradient corresponds to a modified objective function (green) with a minimum where the unmodified objective function has the target first-order saddle point.

3.9 Direct Optimization Generalized Mode Following

The GMF method presented in this thesis and the original articles I and II within is a generalization of the minimum mode following (MMF) method [57–60] which is used to locate first-order saddle points on the surface defined by the electronic energy as a function of the positions of the nuclei. First-order saddle points connecting two minima are used to generate hyperplanar transition states within the harmonic approximation to transition state theory when estimating the rates of atomic rearrangements, such as chemical reactions [61, 62]. The MMF method is illustrated in fig. 3.3. A modified gradient, $\boldsymbol{g}_{\mathrm{mod}}$, is evaluated by inverting the projection of the total gradient, $\boldsymbol{g}$, along the eigenvector corresponding to the lowest eigenvalue of the Hessian, $\boldsymbol{v}_1$, according to

$$\boldsymbol{g}_{\mathrm{mod}}^{\mathrm{MMF}} = \begin{cases} \boldsymbol{g} - 2\boldsymbol{v}_1\boldsymbol{v}_1^{\mathrm{T}}\boldsymbol{g} & \text{if } \lambda_1 < 0\,, \\ -\boldsymbol{v}_1\boldsymbol{v}_1^{\mathrm{T}}\boldsymbol{g} & \text{if } \lambda_1 \geq 0\,. \end{cases} \tag{3.43}$$

If the lowest eigenvalue of the Hessian, λ_1, is non-negative, only the negative projection of the gradient along the eigenvector corresponding to the lowest eigenvalue of the Hessian is followed to enhance the stability of the method. This modified gradient corresponds to an unknown modi-

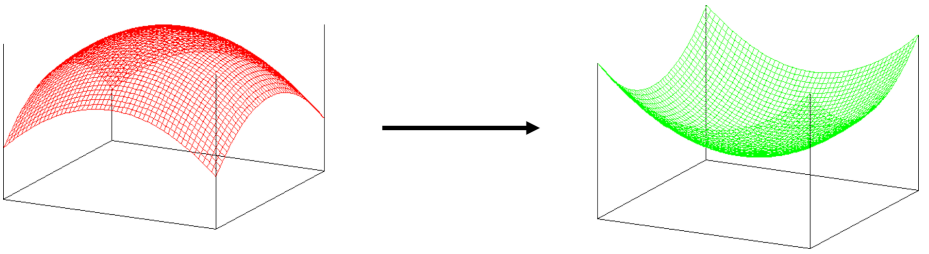

Figure 3.4. Schematic illustration of the GMF method. The objective is to find the second-order saddle point (equivalent to a maximum) of the objective function (red). A modified gradient is evaluated by inverting the sum of the projections of the total gradient on the eigenvectors corresponding to the lowest two eigenvalues of the Hessian. This modified gradient corresponds to a modified objective function (green) with a minimum where the unmodified objective function has the target second-order saddle point.

fied objective function with a minimum where the unmodified objective function has the target first-order saddle point. As a result, this modified gradient is used in combination with robust and efficient minimization techniques such as the L-BFGS method, while ensuring convergence to a first-order saddle point.

In order to use the MMF method in the context of DO electronic structure calculations, a generalization to saddle points of arbitrary order is required. The GMF method is illustrated in fig. 3.4. The generalized modified gradient is evaluated by inverting the sum of the projections of the total gradient along the eigenvectors corresponding to the lowest n eigenvalues of the Hessian as

$$\boldsymbol{g}^{\mathrm{mod}} = \begin{cases} \boldsymbol{g} - 2\sum_{i=1}^{n} \boldsymbol{v}_i \boldsymbol{v}_i^{\mathrm{T}} \boldsymbol{g} & \text{if } \lambda_n < 0\,, \\ -\sum_{\substack{i=1 \\ \lambda_i \geq 0}}^{n} \boldsymbol{v}_i \boldsymbol{v}_i^{\mathrm{T}} \boldsymbol{g} & \text{if } \lambda_n \geq 0\,. \end{cases} \tag{3.44}$$

If any of the lowest n eigenvalues of the Hessian are non-negative, only the negative sum of the projections of the gradient along those eigenvectors corresponding to non-negative eigenvalues is followed to increase

the stability of the method. A finite difference generalized Davidson method [63, 64] is used to evaluate the lowest n eigenpairs of the electronic Hessian.

Estimating the saddle point order of the solution to target with the GMF method can be challenging when the saddle point search is initialized by performing an excitation with respect to the ground state solution. An improved initial guess is obtained if a constrained minimization is performed first in the subspace of orbital rotations excluding the orbitals involved in the excitation.

4 Summary of Original Articles

4.1 Original Article I

4.1.1 Summary

Article I presents the direct optimization generalized mode following (DO-GMF) method and addresses the first research question posed in sec. 1.2.

The flowchart of the DO-GMF algorithm is shown in fig. 4.1. This implementation uses a finite difference generalized Davidson method to evaluate the eigenvectors corresponding to the lowest n eigenvalues of the electronic Hessian, where n is the saddle point order of the target excited electronic state. Initially, a diagonal approximation $\mathbf{D}$ of the electronic Hessian is calculated following eq. 3.16. Next, the generalized Davidson method is started by forming an initial guess for the Krylov subspace $\mathbf{K}$ consisting of n unit column vectors $\boldsymbol{k}_i$ along the orbital rotations corresponding to the lowest n elements of $\mathbf{D}$. $\mathbf{K}$ is orthonormalized by applying the modified Gram-Schmidt procedure after adding a small amount of numerical noise to prevent near-orthogonality between the initial guess vectors and the target eigenvectors which would slow down convergence of the Davidson method. The effect of the electronic Hessian $\mathscr{H}$ on $\mathbf{K}$ is evaluated by the forward finite difference approximation

$$\mathscr{H}\boldsymbol{k}_i \approx \frac{\nabla E\left(\mathbf{C}e^{h\boldsymbol{\kappa}[\boldsymbol{k}_i]}\right) - \nabla E\left(\mathbf{C}\right)}{h}, \tag{4.1}$$

with $\boldsymbol{\kappa}[\boldsymbol{k}_i]$ being the anti-Hermitian matrix containing the elements of the i^{th} vector of the Krylov subspace, $\boldsymbol{k}_i$, in its upper triangular part and h being the size of the finite difference step. By using eq. 4.1, the Rayleigh matrix $\mathbf{K}^T\mathscr{H}\mathbf{K}$, a representation of the eigenvalue problem in a reduced space, is evaluated and diagonalized to obtain the approximate

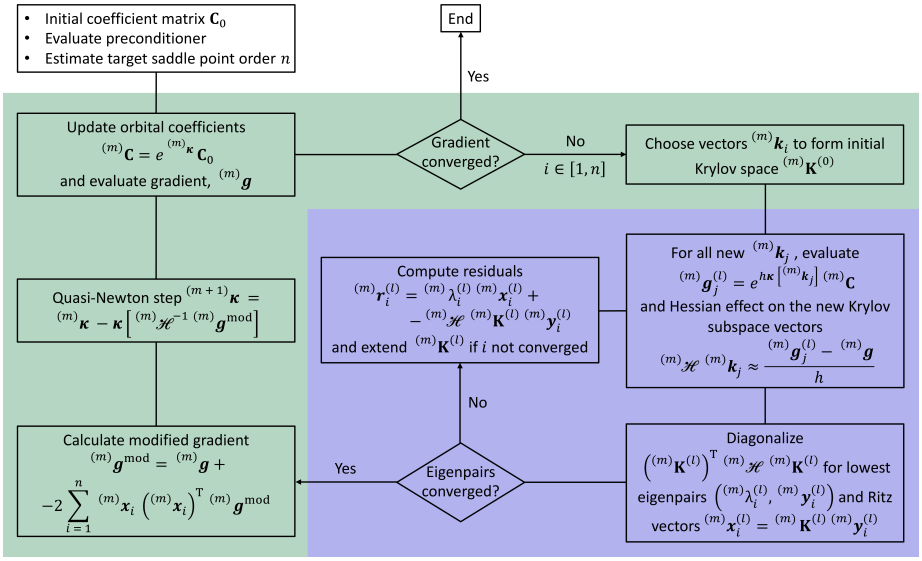

Figure 4.1. Flowchart of the DO-GMF algorithm. The approach consists of a DO outer loop (green) using the exponential transformation and a QN step with a modified gradient determined in a partial Hessian diagonalization inner loop (blue) using the generalized Davidson method. Taken from original article I.

n lowest eigenpairs $(\lambda_i, \boldsymbol{y}_i)$ in the reduced space. The representation of the approximate eigenvectors in the full space, the Ritz vectors $\boldsymbol{x}_i = \mathbf{K}\boldsymbol{y}_i$ and their residual vectors $\boldsymbol{r}_i = (\lambda_i \mathbf{I} - \mathscr{H})\boldsymbol{x}_i$ are calculated. $\mathbf{K}$ is extended with the n preconditioned residual vectors, where the preconditioners are $\mathbf{P}_i = (\lambda_i \mathbf{I} - \mathbf{D})^{-1}$. The required diagonalization is computationally inexpensive since all $\mathbf{P}_i^{-1}$ are diagonal. The preconditioners are required to be negative-definite to ensure convergence of the generalized Davidson method to the lowest eigenpairs. The residual vectors are used to monitor convergence of the method since they tend to zero with convergence. With the converged lowest eigenvectors of the Hessian, the modified gradient is evaluated according to eq. 3.44 and a minimization step is taken.

An example of a case where multiple solutions emerge from one in a minimal-basis hydrogen model discussed in sec. 3.8 is shown in fig. 4.2. The convergence behaviors of the DO-GMF method and the regular DO approach combined with the maximum overlap method (DO-MOM) are compared for a separate calculation of the doubly excited electronic state of the molecule for a distance between the atoms where multiple solutions for this excited state exist and a consecutive evaluation of the energy curve of this excited state starting from a distance between the atoms where only one solution exists and moving through the point at which multiple solutions emerge. In the first calculation shown in fig. 4.2a, a single point calculation is carried out at a distance between the atoms of 0.4 Å beyond the minimum energy distance, r_e using the S_0^S solution as the initial guess by performing a double excitation from the HOMO to the LUMO in both spin channels. A saddle point order of 2 is targeted in the DO-GMF calculation. Even though this initial guess is located at the first-order saddle point corresponding to the S_2^S solution within numerical accuracy, the DO-GMF method climbs up the energy surface and converges to a second-order saddle point corresponding to a spatially symmetry-broken S_2^{BS} solution. The DO-MOM calculation, on the other hand, immediately converges to the first-order saddle point and thus, does not manage to break the spatial symmetry. The second example in fig. 4.2 is a consecutive evaluation of the binding curve of the S_2 electronic state starting with an excited ground state initial guess at r_e and increasing the distance between the hydrogen atoms by 0.1 Å in five calculations that are initialized from the converged excited state

solution at the previous geometry. The point at which multiple solutions emerge is passed between r_e and $r_e + 0.1$ Å, leading to two solutions emerging from a single second-order saddle point: a first-order saddle point corresponding to S_2^S and a pair of degenerate second-order saddle points corresponding to S_2^{BS}. Since the first-order saddle point is located exactly where the one existing solution is located at the previous geometry, DO-MOM converges to this symmetry-conserving solution, similarly to the single point case. DO-GMF immediately climbs up in energy to one of the two second-order saddle points breaking the spatial symmetry.

Charge transfer excitations typically involve a large rearrangement of the electron density with respect to the ground state, making these excitations especially prone to variational collapse. The HOMO $\rightarrow$ LUMO excited state of the twisted *N*-phenylpyrrole molecule is an example of a charge transfer excited state where variational collapse cannot be avoided with MOM. Targeting a sixth-order saddle point at the PBE/cc-pVDZ [65–67] level of theory, the DO-GMF method avoids variational collapse by construction.

In conclusion, research question 1 in sec. 1.2 is answered:

Multiple emerging solutions in consecutive variational time-independent density functional calculations of excited electronic states at different positions of the nuclei can be differentiated by their saddle point orders on the surface defined by the electronic degrees of freedom. Based on the saddle point order, the desired solution can be targeted with the newly developed direct optimization generalized mode following method and variational collapse is prevented by construction.

4.2 Original Article II

4.2.1 Summary

Article II presents an extension of the DO-GMF method for Perdew-Zunger self-interaction corrected density functionals and addresses the second research question posed in sec. 1.2.

By adding one electron to the hydrogen model system discussed in sec. 3.8, the anionic H_2^- system is obtained. The electron is placed in the

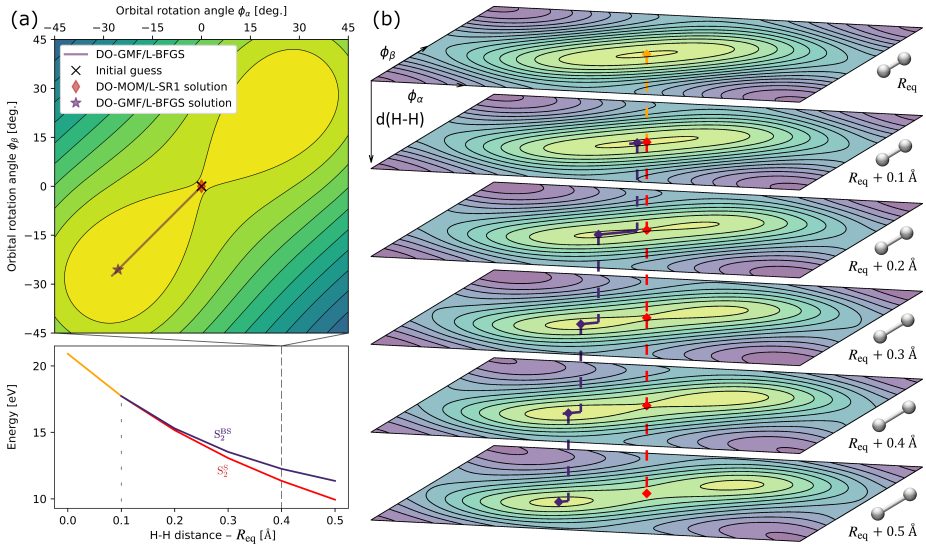

Figure 4.2. Calculations of the doubly excited singlet state of the minimal-basis H_2 molecule illustrating the way DO-GMF converges on the higher-energy, symmetry-broken solution and provides the right potential energy curve, while DO-MOM converges on the symmetry-pure solution. (a) At a bond length of $R_{eq} + 0.4$ Å, symmetry breaking can occur, but when the starting point ($\times$) corresponds to a double excitation of the symmetry-pure ground state solution, S_0^S, the DO-MOM calculation converges on a first-order saddle point (red diamond) corresponding to the symmetry-pure solution, S_2^S, as it is nearly at the same location. The DO-GMF calculation, however, climbs up (purple line) to one of the two equivalent second-order saddle points (purple diamond), corresponding to a symmetry-broken solution, S_2^{BS}. The curves in the lower graph show the variation of the energy with the H-H distance for the S_2^{BS} (purple) and S_2^S (red) states, while for short distance, only the symmetry-pure solution exists (orange). (b) Sequential calculations for six bond lengths spaced 0.1 Å apart using DO-GMF (purple) and DO-MOM (red). The first calculation starts at R_{eq} in the same way as in (a), while subsequent calculations use the orbitals obtained for the previous H-H distance (indicated by dashed lines) as input. Even after the onset of symmetry breaking at $R_{eq} + 0.1$ Å, DO-MOM keeps converging on the symmetry-pure solution, S_2^S, a first-order saddle point, while DO-GMF converges consistently on a second-order saddle point corresponding to a symmetry-broken solution, S_2^{BS}, and thereby provides the right energy curve for dynamics in the excited state. Taken from original article I.

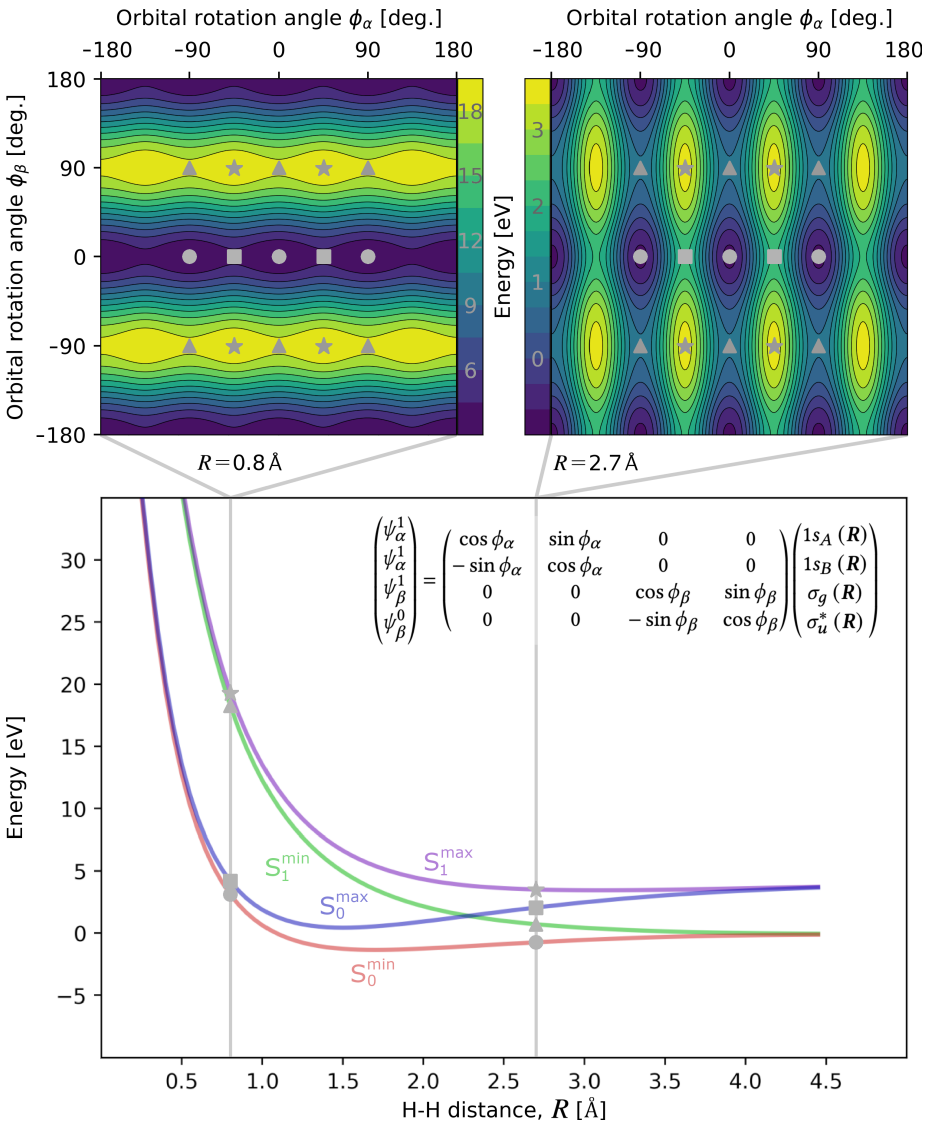
Orbital rotation angle ϕ_α [deg.]
-180
-90
0
90
180
Orbital rotation angle ϕ_β [deg.]
Energy [eV]
$R = 0.8$ Å
$R = 2.7$ Å
$\begin{pmatrix} \psi_\alpha^1 \\ \psi_\alpha^1 \\ \psi_\beta^1 \\ \psi_\beta^0 \end{pmatrix} = \begin{pmatrix} \cos\phi_\alpha & \sin\phi_\alpha & 0 & 0 \\ -\sin\phi_\alpha & \cos\phi_\alpha & 0 & 0 \\ 0 & 0 & \cos\phi_\beta & \sin\phi_\beta \\ 0 & 0 & -\sin\phi_\beta & \cos\phi_\beta \end{pmatrix} \begin{pmatrix} 1s_A(\boldsymbol{R}) \\ 1s_B(\boldsymbol{R}) \\ \sigma_g(\boldsymbol{R}) \\ \sigma_u^*(\boldsymbol{R}) \end{pmatrix}$
$S_1^{\min}$
$S_1^{\max}$
$S_0^{\max}$
$S_0^{\min}$
H-H distance, $\boldsymbol{R}$ [Å]

Figure 4.3. Energy as a function of bond length, R, for the two states that can be obtained for the minimal-basis H_2^- ion where two electrons are in the α and one electron is in the β spin channel. The orbitals are related by rotation angles ϕ_α, mixing two occupied orbitals, and ϕ_β, mixing an occupied and a virtual orbital, with respect to the orbitals of the ground state solution, $S_0^{\min}$, corresponding to the localized orbitals $1s_A$ and $1s_B$ at H_A and H_B, respectively, in the α channel and the delocalized bonding and antibonding orbitals σ_g and σ_u^*, respectively, in the β channel. The S_1 state is obtained by a single excitation in the β spin channel with respect to S_0. The superscripts 0 and 1 indicate the orbital occupation, while the superscripts min and max indicate whether a minimum or maximum of the self-interaction error has been found, respectively. The left contour graph corresponds to a bond length of $R = 0.8$ Å. There, $S_0^{\min}$ corresponds to a minimum (circles), while $S_0^{\max}$ (squares) and $S_1^{\min}$ (triangles) correspond to first-order saddle points with the direction of negative curvature along ϕ_α and ϕ_β, respectively. $S_1^{\max}$is represented by a second-order saddle point. The curvature of the surface along ϕ_α at $S_0^{\min}$ is much smaller than along ϕ_β. The right contour graph corresponds to a stretched bond length of $R = 2.7$ Å. The locations of the stationary points persist, but the curvature changes significantly with the curvature along ϕ_α now being much larger than along ϕ_β. Taken from original article II.

α spin channel leading to this spin channel now being fully occupied and the orbital rotation ϕ_α mixing two occupied orbitals. The energy is evaluated with the PBE functional and SIC, so the dependence of the electronic energy on ϕ_α is entirely due to the SIC contribution. Figure 4.3 shows the energy curves as a function of the distance between the hydrogen atoms, R, that can be obtained for this system as well as the electronic energy surface as a function of the two electronic degrees of freedom for distances of $R = 0.8$ Å and $R = 2.7$ Å. The electronic degrees of freedom, ϕ_α and ϕ_β are defined by

$$\begin{pmatrix} \psi_\alpha^1 \\ \psi_\alpha^1 \\ \psi_\beta^1 \\ \psi_\beta^0 \end{pmatrix} = \begin{pmatrix} \cos\phi_\alpha & \sin\phi_\alpha & 0 & 0 \\ -\sin\phi_\alpha & \cos\phi_\alpha & 0 & 0 \\ 0 & 0 & \cos\phi_\beta & \sin\phi_\beta \\ 0 & 0 & -\sin\phi_\beta & \cos\phi_\beta \end{pmatrix} \begin{pmatrix} 1s_A(R) \\ 1s_B(R) \\ \sigma_g(R) \\ \sigma_u^*(R) \end{pmatrix}, \quad (4.2)$$

which differs from eq. 3.25 in the full occupation of the α spin channel and the reference orbitals for ϕ_α. The latter are again chosen as the ground state optimal orbitals, however in this case, SIC leads to the optimal orbitals in the α spin channel being fully localized 1s orbitals because the SIE is minimized in this way. There are two electronic states in this model. The ground state is weakly bound. The other electronic state is an excited state obtained by performing an excitation between the HOMO and LUMO in the β spin channel, with a monotonically decreasing energy curve. The locations of the stationary points on the electronic energy surface are identical for both values of R. The ground state solution, $S_0^{\min}$, corresponds to a minimum placed at the origin. Setting $\phi_\beta = \pm 90^\circ$ yields a first-order saddle point corresponding to the excited state solution $S_1^{\min}$. Applying $\phi_\alpha = \pm 45^\circ$ fully delocalizes the orbitals in the α spin channel, which leads to maximizing the SIE. As a result, another set of stationary solutions, $S_0^{\max}$ and $S_1^{\max}$, is observed different from $S_0^{\min}$ and $S_1^{\min}$ only in maximizing the SIE instead of minimizing it. Hence the SIE-minimizing and SIE-maximizing solutions show qualitatively similar energy curves. While $S_0^{\min}$ shows a minimum at $R \approx 1.7$ Å, the minimum of $S_0^{\max}$ is located at $R \approx 1.5$ Å. $S_1^{\min}$ and $S_1^{\max}$ are both monotonically decreasing. S_0 and S_1 become degenerate in the dissociation limit, but the energy in the limit differs for the sets depending on whether the SIE is minimized or maximized, due to the difference in the SIE contribution to the energy. In the $R \to 0$ limit, $E_e \to \infty$ and

the SIE vanishes since there is no difference between the localized and delocalized orbital sets, so the two pairs of solutions become identical. The electronic energy surfaces demonstrate that the curvature along the electronic degrees of freedom can change quite drastically. While ϕ_α represents the direction of lowest curvature at $R = 0.8$ Å, at $R = 2.7$ Å, it is ϕ_β.

The point of SIC is to minimize the SIE. Maximizing the SIE along any electronic degrees of freedom thus leads to a spurious solution. Local minimization of the SIE can be ensured by modifying the GMF method such that a minimization is performed in the subspace of oo rotations of $\boldsymbol{\kappa}$, $\boldsymbol{\kappa}_{\mathrm{oo}}$ and the saddle point search is limited to $\boldsymbol{\kappa}_{\mathrm{ov}}$. Since rotations contained in $\boldsymbol{\kappa}_{\mathrm{oo}}$ can dominate the lowest eigenvectors of the electronic Hessian, the lowest eigenvectors obtained with the generalized Davidson method need to be checked for their localization in the $\boldsymbol{\kappa}_{\mathrm{oo}}$ subspace. If an eigenvector is localized more than a threshold t_{oo} in $\boldsymbol{\kappa}_{\mathrm{oo}}$, the eigenvector is discarded and the generalized Davidson procedure continued, targeting the next higher eigenvectors of the Hessian until the desired amount of eigenvectors localized in $\boldsymbol{\kappa}_{\mathrm{ov}}$ is identified. The threshold is evaluated as

$$\left| \sum_{i}^{N_{\mathrm{oo}}} \boldsymbol{v}^T \boldsymbol{u}_i^{\mathrm{oo}} \boldsymbol{u}_i^{\mathrm{oo}} \right| < t_{\mathrm{oo}} \,, \tag{4.3}$$

where N_{oo} is the number of unit vectors $\boldsymbol{u}_i^{\mathrm{oo}}$ of the oo subspace.

In conclusion, research question 2 in sec. 1.2 is answered:

Spurious solutions introduced by Perdew-Zunger self-interaction correction on the energy surface defined by the electronic degrees of freedom are characterized by maximizing the self-interaction error along some electronic degrees of freedom. A strategy is presented to avoid such spurious solutions with the generalized mode following method by performing a minimization in the subspace of occupied-occupied orbital rotation degrees of freedom and following only those eigenvectors of the electronic Hessian up in energy that are localized in the subspace of occupied-virtual orbital rotation degrees of freedom.

4.3 Original Article III

4.3.1 Summary

Article III presents DO calculations of an avoided crossing and conical intersection in the ethylene molecule and addresses the third research question posed in sec. 1.2.

The avoided crossing and the conical intersection of the ethylene molecule obtained with the DO method with the PBE functional are shown in fig. 4.4. SIC is used for the avoided crossing and the results are compared to published multireference configuration interaction singles and doubles (MRCISD) results [68]. Symmetry breaking is allowed in the single-determinant wave functions. The branching space coordinates that lift the degeneracy between the ground electronic state, N, and the valence singly excited electronic state, V, are the torsion angle around the C-C double bond, θ, and the pyramidalization angle, ϕ, of one of the two methylene groups. The obtained conical intersection between the N and V states shows no spurious negative energy gaps, which are often observed with TDDFT [68, 69]. An avoided crossing including the valence doubly excited electronic state, Z, is displayed as the torsion slice along $\phi = 0$. The agreement between the PBE-SIC energy curves and the MRCISD results is near-quantitative.

In conclusion, research question 3 in sec. 1.2 is answered:

Direct optimization methods can provide the correct topology of a conical intersection in the ethylene molecule provided that the single-determinant wave functions are allowed to break the symmetries of the Hamiltonian.

4.3.2 Symmetry Analysis of the Conical Intersection

A symmetry analysis of the electronic wave functions and Slater determinants of the ethylene molecule is presented in article III to obtain multideterminant corrections to the single-determinant wave function energy values calculated with the DO methods. Here, this symmetry analysis is extended to the point group C_S, which contains the conical intersection presented in the article. The degeneracy condition is then used to derive the energy of the multideterminant wave functions at the conical intersection.

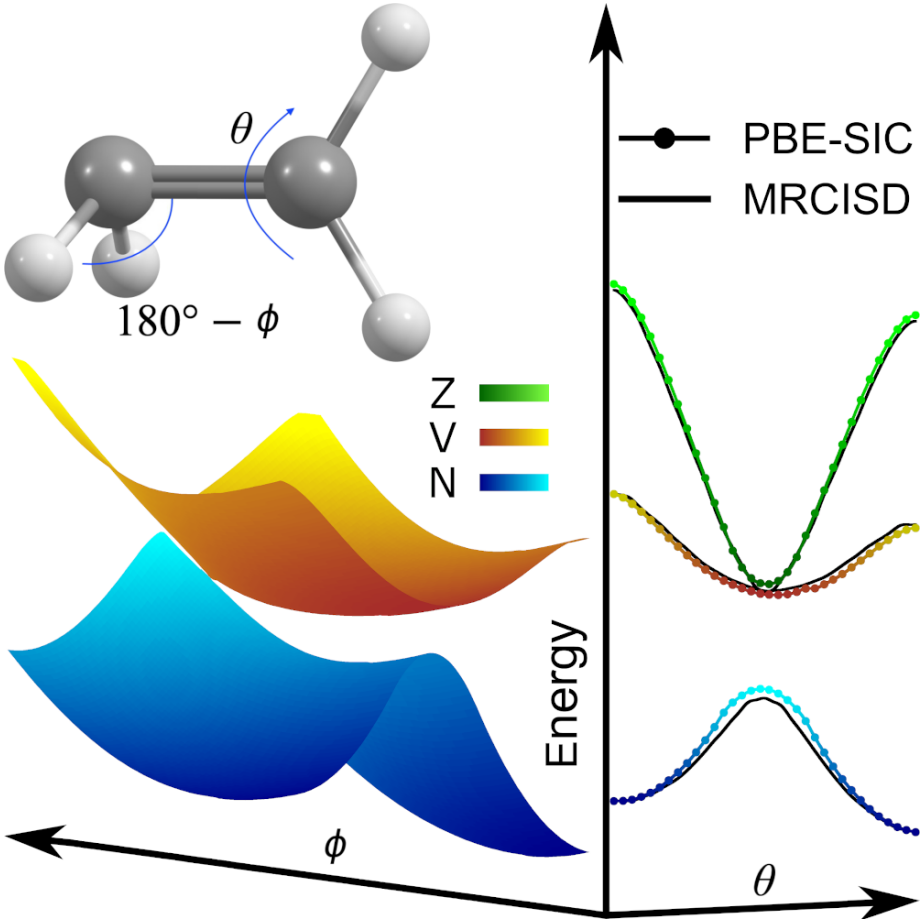

Figure 4.4. Avoided crossing and conical intersection in the ethylene molecule obtained with the PBE functional by allowing for symmetry breaking in the single-determinant wave functions. SIC is used for the avoided crossing and the results are compared to published multireference configuration interaction singles and doubles (MRCISD) results [68]. The illustration of the molecule shows the branching space coordinates that lift the degeneracy between the ground electronic state, N, and the valence singly excited electronic state, V, where θ is the torsion angle around the C-C double bond and ϕ is the pyramidalization angle of one of the two methylene groups. The conical intersection is shown by the energy surfaces of the N and V states. No spurious negative energy difference between the intersecting surfaces is observed. The avoided crossing is displayed as the torsion slice of the surfaces along $\phi = 0$ and the valence doubly excited electronic state, Z, is included as well. Near-quantitative agreement of the PBE-SIC energy curves with the MRCISD results is observed. Taken from original article III.

Table 4.1. Symmetry characters of the frontier orbitals of the ethylene molecule in the C_S point group.

	E	σ_h	
p	1	-1	A"
p'	1	1	A'

C_S Point Group

The C_S point group symmetry is obtained from the twisted D_{2d} geometry by increasing the pyramidalization ϕ of one of the methylene groups from 0°. This point group is defined for $\theta = \{0, 90^\circ\}$ and all values of ϕ. The set of frontier orbitals in this point group has considerable p-orbital character. While the orbitals are non-bonding, they are not degenerate in this point group due to the lack of symmetry axes. Table 4.1 collects the symmetry characters of this set. These orbitals are denoted by p and p'. There are six different determinants which can be formed with the frontier orbital set:

$$
\begin{aligned}
D_1 &= |p_1 \alpha_1 p_2 \beta_2\rangle\,, \\
D_2 &= |p'_1 \alpha_1 p'_2 \beta_2\rangle\,, \\
D_3 &= |p_1 \alpha_1 p'_2 \beta_2\rangle\,, \\
D_4 &= |p'_1 \alpha_1 p_2 \beta_2\rangle\,, \\
D_5 &= |p_1 \alpha_1 p'_2 \alpha_2\rangle\,, \\
D_6 &= |p_1 \beta_1 p'_2 \beta_2\rangle\,.
\end{aligned}
$$

The determinants are antisymmetrized. The first two determinants are singlet determinants, the second pair consists of spin impure determinants, and the last two determinants are triplet determinants. The characters of these determinants are displayed in table 4.2. As the spatial parts of D_5 and D_6 are identical to that of D_3, they are excluded in this analysis. Since the spin parts between the spin-antisymmetric singlet and spin-impure determinants and the spin-symmetric triplet determinants as well as the spin parts of the triplet determinants with different values of s_z integrate to zero,

$$
\begin{aligned}
&\langle D_1|\hat{H}|D_5\rangle = \langle D_2|\hat{H}|D_5\rangle = \langle D_3|\hat{H}|D_5\rangle = \langle D_4|\hat{H}|D_5\rangle = \langle D_1|\hat{H}|D_6\rangle \\
&= \langle D_2|\hat{H}|D_6\rangle = \langle D_3|\hat{H}|D_6\rangle = \langle D_4|\hat{H}|D_6\rangle = \langle D_5|\hat{H}|D_6\rangle = 0\,.
\end{aligned}
$$

Table 4.2. Symmetry characters of the Slater determinants of the ethylene molecule formed with the frontier orbitals in the C_S point group.

	E	σ_h	
D_1	1	1	A'
D_2	1	1	A'
D_3	1	-1	A''
D_4	1	-1	A''

The spin parts between different singlet and spin-impure determinants integrate to unity, so a spatial symmetry analysis is required to show which off-diagonal Hamiltonian matrix elements in the set of singlet and spin-impure determinants vanish.

For the first two determinants,

$$\hat{E}\,\langle D_1|\hat{H}|D_2\rangle = \langle D_1|\hat{H}|D_2\rangle\,,$$
$$\hat{\sigma}_h\,\langle D_1|\hat{H}|D_2\rangle = \langle D_1|\hat{H}|D_2\rangle\,.$$

It follows that

$$\langle D_1|\hat{H}|D_2\rangle \neq 0.$$

For the last two singlet determinants,

$$\hat{E}\,\langle D_3|\hat{H}|D_4\rangle = \langle D_3|\hat{H}|D_4\rangle\,,$$
$$\hat{\sigma}_h\,\langle D_3|\hat{H}|D_4\rangle = \langle(-D_3)|\hat{H}|(-D_4)\rangle = \langle D_3|\hat{H}|D_4\rangle\,.$$

It follows that

$$\langle D_3|\hat{H}|D_4\rangle \neq 0.$$

For D_1 and D_4,

$$\hat{\sigma}_h\,\langle D_1|\hat{H}|D_4\rangle = \langle D_1|\hat{H}|(-D_4)\rangle = -\langle D_1|\hat{H}|D_4\rangle\,.$$

Since the integrals must adhere to the point group symmetry of the system, D_2 transforms as D_1 and D_3 transforms as D_4, it follows that

$$\langle D_1|\hat{H}|D_4\rangle = -\langle D_1|\hat{H}|D_4\rangle = \langle D_2|\hat{H}|D_4\rangle = -\langle D_2|\hat{H}|D_4\rangle$$
$$= \langle D_1|\hat{H}|D_3\rangle = -\langle D_1|\hat{H}|D_3\rangle = \langle D_2|\hat{H}|D_3\rangle = -\langle D_2|\hat{H}|D_3\rangle = 0.$$

Table 4.3. Symmetry characters of the multideterminant wave functions formed with the frontier orbitals of the ethylene molecule in the C_S point group.

	E	σ_h	
Ψ_1	1	-1	A"
Ψ_2	1	1	A'
Ψ_3	1	-1	A"
Ψ_4	1	1	A'

The antisymmetric many-body wave functions are

$$\Psi_1 = \frac{1}{\sqrt{2}}\left(p_1 p_2' - p_1' p_2\right) \times \begin{cases} \alpha_1\alpha_2 \\ \frac{1}{\sqrt{2}}\left(\alpha_1\beta_2 + \beta_1\alpha_2\right) \\ \beta_1\beta_2 \end{cases},$$

$$\Psi_2 = \frac{1}{2}\left(p_1 p_2 + p_1' p_2'\right)\left(\alpha_1\beta_2 - \beta_1\alpha_2\right),$$

$$\Psi_3 = \frac{1}{2}\left(p_1 p_2' + p_1' p_2\right)\left(\alpha_1\beta_2 - \beta_1\alpha_2\right).$$

$$\Psi_4 = \frac{1}{2}\left(p_1 p_2 - p_1' p_2'\right)\left(\alpha_1\beta_2 - \beta_1\alpha_2\right).$$

Their characters and irreducible representations are shown in table 4.3. A similar analysis as for the D_{2h} point group shown in article III yields the result

$$\langle\Psi_1|\hat{H}|\Psi_1\rangle = \langle D_5|\hat{H}|D_5\rangle \tag{4.4}$$

$$\langle\Psi_2|\hat{H}|\Psi_2\rangle = \frac{1}{2}\left(\langle D_1|\hat{H}|D_1\rangle + \langle D_2|\hat{H}|D_2\rangle\right) + \langle p_1 p_2|\, r_{12}^{-1}\,|p_1' p_2'\rangle \tag{4.5}$$

$$\langle\Psi_3|\hat{H}|\Psi_3\rangle = 2\langle D_3|\hat{H}|D_3\rangle - \langle D_5|\hat{H}|D_5\rangle \tag{4.6}$$

$$\langle\Psi_4|\hat{H}|\Psi_4\rangle = \frac{1}{2}\left(\langle D_1|\hat{H}|D_1\rangle + \langle D_2|\hat{H}|D_2\rangle\right) - \langle p_1 p_2|\, r_{12}^{-1}\,|p_1' p_2'\rangle\,. \tag{4.7}$$

Note that the two-electron integral splitting the energy of the wave functions Ψ_2 and Ψ_4 around the average energy of the determinants D_1 and D_2 is never negligible in the C_S point group since the determinant energy

values are always close. Equation 4.6 is the well-known spin-purification formula for open-shell singlet excited states.

Conical Intersection

A conical intersection between Ψ_2 and Ψ_3 is obtained at $\theta = 90^\circ$ and $\phi \approx 110^\circ$, depending on the method used to calculate the wave functions and their energy values. A conical intersection occurs if the energy difference ΔV between the adiabatic electronic states obtained by diagonalizing the diabatic Hamiltonian matrix, vanishes, i.e.

$$\mathbf{H} = \begin{pmatrix} \langle\Psi_2|\hat{H}|\Psi_2\rangle & \langle\Psi_2|\hat{H}|\Psi_3\rangle \\ \langle\Psi_2|\hat{H}|\Psi_3\rangle & \langle\Psi_3|\hat{H}|\Psi_3\rangle \end{pmatrix}$$
$$\Delta V = \sqrt{\left(\langle\Psi_2|\hat{H}|\Psi_2\rangle - \langle\Psi_3|\hat{H}|\Psi_3\rangle\right)^2 + 4\langle\Psi_2|\hat{H}|\Psi_3\rangle} \stackrel{!}{=} 0\,.$$

Since the Hamiltonian is a Hermitian operator, its matrix elements are real, thus the two conditions

$$\langle\Psi_2|\hat{H}|\Psi_3\rangle \stackrel{!}{=} 0\,,$$
$$\langle\Psi_2|\hat{H}|\Psi_2\rangle \stackrel{!}{=} \langle\Psi_3|\hat{H}|\Psi_3\rangle$$

are derived. The former condition is satisfied in the point group C_S, as

$$\langle\Psi_2|\hat{H}|\Psi_3\rangle = \hat{\sigma}_h\langle\Psi_2|\hat{H}|\Psi_3\rangle = \langle\Psi_2|\hat{H}|(-\Psi_3)\rangle = -\langle\Psi_2|\hat{H}|\Psi_3\rangle = 0\,,$$

i.e. this condition is fulfilled by fixing the torsion θ to 90°. The second condition specifies the pyramidalization ϕ.

Equalizing (4.5) and (4.6) yields

$$\langle D_1|\hat{H}|D_2\rangle = -\frac{1}{2}\left(\langle D_1|\hat{H}|D_1\rangle + \langle D_2|\hat{H}|D_2\rangle\right) + 2\langle D_3|\hat{H}|D_3\rangle - \langle D_5|\hat{H}|D_5\rangle\,. \tag{4.8}$$

Substitution of (4.8) in (4.5) and (4.7) allows the evaluation of

$$\langle\Psi_2|\hat{H}|\Psi_2\rangle = 2\langle D_3|\hat{H}|D_3\rangle - \langle D_5|\hat{H}|D_5\rangle$$
$$\langle\Psi_4|\hat{H}|\Psi_4\rangle = \langle D_1|\hat{H}|D_1\rangle + \langle D_2|\hat{H}|D_2\rangle - 2\langle D_3|\hat{H}|D_3\rangle + \langle D_5|\hat{H}|D_5\rangle\,,$$

providing the means to evaluate all wave function energy values from the single-determinant energy values at the conical intersection.

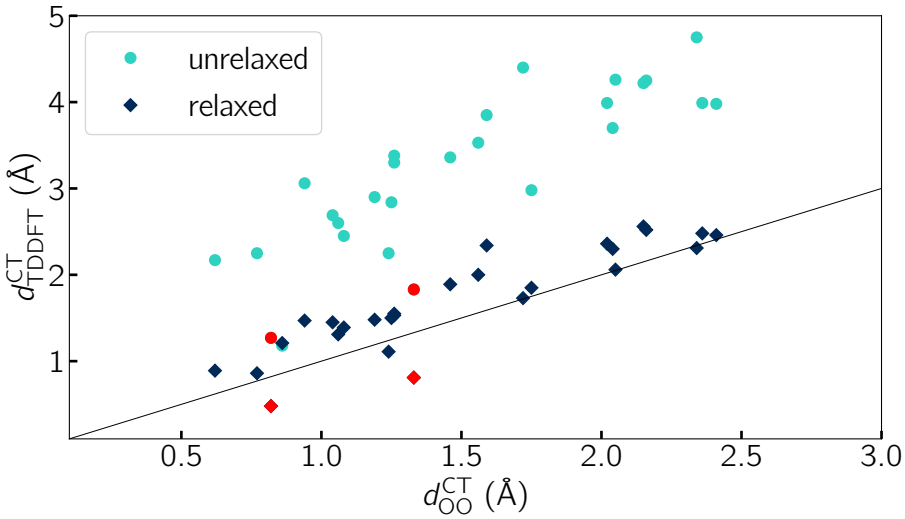

Figure 4.5. Comparison between charge transfer distances of excited states of organic molecules obtained from time-dependent and orbital optimized calculations using the PBE functional. The black line represents one-to-one correspondence. TDDFT overestimates the charge transfer distance both when using only the unrelaxed part of the difference density matrix and when employing the full, relaxed difference density matrix obtained through the Z-vector approach. The red points correspond to excitations where TDDFT gives mixing with Rydberg states. Taken from original article IV.

4.4 Original Article IV

4.4.1 Summary

Article IV presents a benchmark of DO methods against linear-response adiabatic time-dependent DFT (TDDFT) with respect to charge transfer excited states of organic molecules and addresses the fourth research question posed in sec. 1.2.

The DO calculations presented in this article employ a constrained minimization technique, where the energy is minimized in the subspace of orbital rotations excluding the orbitals between which the excitation is performed followed by an unconstrained optimization. The performance of the methods is assessed with the LDA and the BLYP [70, 71] and

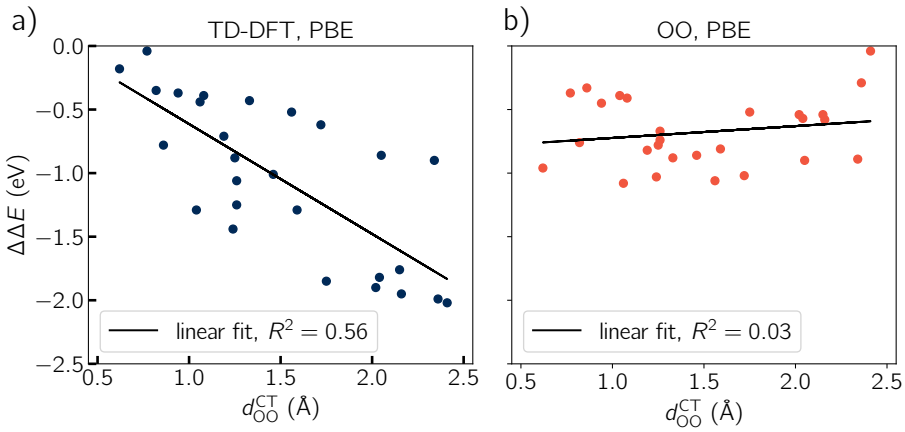

Figure 4.6. Error on the excitation energy of intramolecular charge transfer states of organic molecules relative to theoretical best estimates [73] for TDDFT and orbital optimized calculations as a function of the charge transfer distance, d_{OO}^{CT}. The calculations use the PBE functional and d_{OO}^{CT} is evaluated from the spin-mixed orbital optimized excited state solution. The black lines represent linear regression fits. The error of TDDFT increases with the charge transfer distance (R^2 of the fit of 0.56), while no correlation between the extent of charge transfer and the accuracy of the computed excitation energy is found for the orbital optimized calculations (R^2 of 0.03). Taken from original article IV.

PBE [47, 48] functionals and the aug-cc-pVDZ [65–67] basis set for a set of 27 charge transfer excitations in 15 organic molecules. Charge transfer distances computed using the electron density difference of the ground and excited states [72] are compared and generally found to be smaller for the DO calculations than for the time-dependent calculations, even when the perturbative orbital relaxation effect is taken into account, as shown in fig. 4.5.

The absolute error of the excitation energy of TDDFT is found to increase with the charge transfer distance up to ca. 2 eV, while no correlation is observed for the DO calculations, where the mean absolute error is ca. 0.7 eV. This result outperforms TDDFT even when local and global hybrid functionals are used for excitations with long-range charge transfer character. The correlation of the excitation energy error with the charge transfer distance is shown in fig. 4.6, while the mean absolute errors

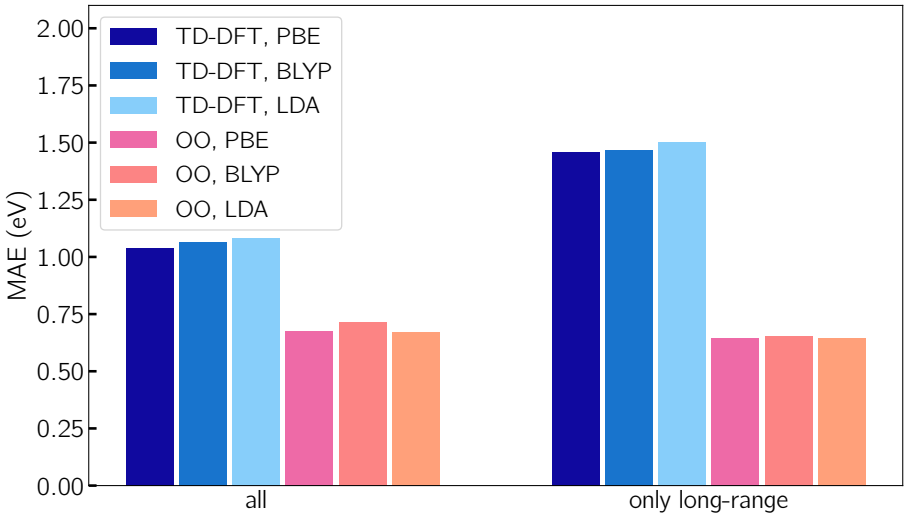

Figure 4.7. Mean absolute error (MAE) on the excitation energy of charge transfer states of organic molecules relative to theoretical best estimates [73] for orbital optimized and TDDFT calculations. The orbital optimized approach yields on average smaller errors than TDDFT. The improvement is most significant for the long-range charge transfer excitations ($d^{\mathrm{CT}} > 1.5\,\text{Å}$, as evaluated from the spin-mixed orbital optimized excited state solution). Taken from original article IV.

are illustrated in fig. 4.7. Exemplary calculations with the global hybrid functional B3LYP [71, 74, 75] and the range-separated hybrid functional CAM-B3LYP [76] are performed as well. The inclusion of exact exchange in the XC functional is found not to impact the charge transfer distance much, while improving the excitation energy.

In conclusion, research question 4 in sec. 1.2 is answered:

Variational time-independent direct orbital optimization methods outperform linear-response time-dependent density functional theory in calculations of the excitation energy of charge transfer states of organic molecules. While the time-dependent calculations tend to perform more poorly the larger the extend of charge transfer of the excited state, no such correlation is observed for the variational methods.

4.5 Original Article V

4.5.1 Summary

Article V presents DO calculations of the negatively charged nitrogen-vacancy center in diamond and addresses the fifth research question posed in sec. 1.2.

The DO results with the LDA, the PBE GGA, and the TPSS [82] and r^{2}SCAN [83] meta GGA functionals are compared to high-level many-body results [77–81] in fig. 4.8. The computations employ a 511-atoms periodic model. The order of electronic states obtained with DO regardless of which functional is used is ${}^3A_2 < {}^1E < {}^1A_1 < {}^3E$ in qualitative agreement with the many-body calculations. With the r^{2}SCAN functional, the agreement with the theoretical best estimate, beyond-RPA quantum embedding [77], is near-quantitative, with the largest absolute deviation being below 0.06 eV. These results are particularly important because several previous DFT calculations have given incorrect ordering of the excited states and statements have been made in the literature that DFT could not be applied to this system because of the multireference nature of the singlet states [79, 84, 85].

Zero phonon line (ZPL) DO calculations are compared to experiment in fig. 4.9. The ZPL is obtained computationally by taking the energy

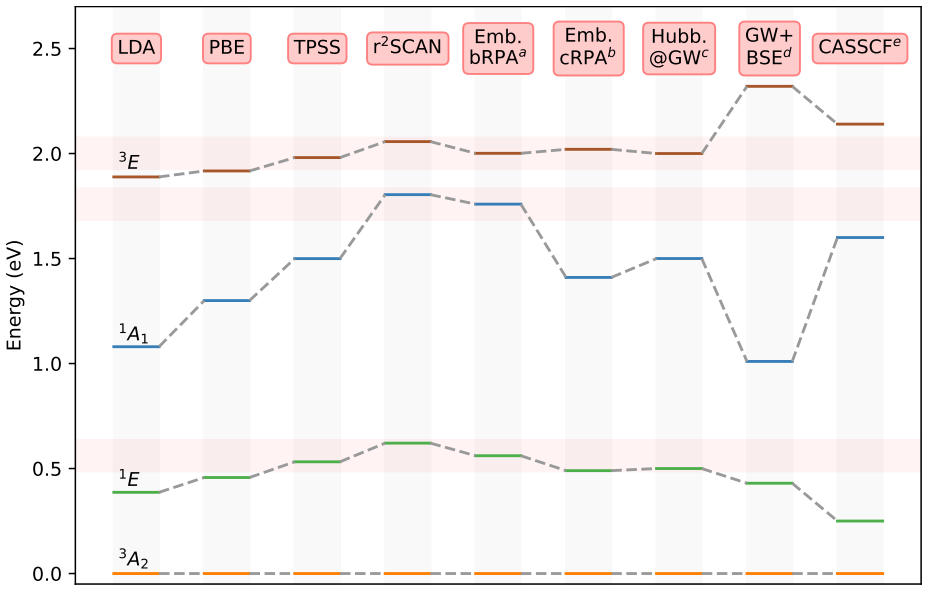

Figure 4.8. Energy of vertical excitations relative to the triplet ground state of the NV^- center in diamond obtained with variational calculations using different local and semilocal density functional approximations, and comparison with results of previous calculations based on many-body approaches: periodic quantum embedding beyond the random phase approximation, beyond-RPA (bRPA) [77], constrained RPA (cRPA) [78], extended Hubbard model fitted to GW calculations [79], periodic GW + Bethe-Salpeter equation (BSE) [80], and molecular cluster complete active space self-consistent field (CASSCF) [81] calculations. The red horizontal shadings span ± 0.075 eV around the values obtained with the beyond-RPA quantum embedding results [77], which are taken to give the best theoretical estimates. The r^{2}SCAN functional gives results that are remarkably close, the largest deviation being below 0.06 eV. All four density functionals used here give the correct ordering of the energy levels of the electronic states. [a]Ref. [77], [b]Ref. [78], [c]Ref. [79], [d]Ref. [80] [e]Ref. [81].

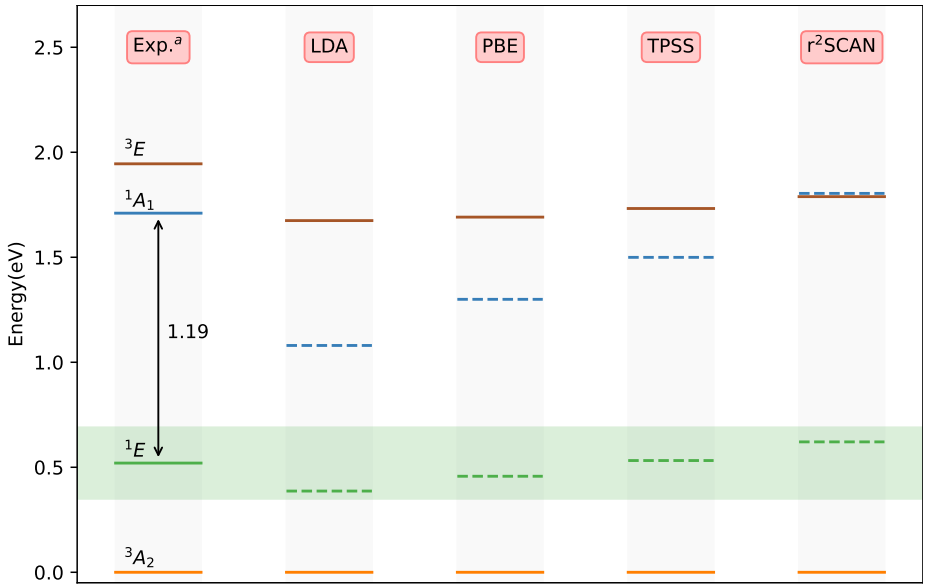

Figure 4.9. Energy of ZPL excitations (solid lines) of the NV^- center in diamond obtained experimentally and from variational calculations using four density functionals, as well as the energy of vertical excitations (dashed lines, same values as in Figure 4.8) to the singlet states where energy lowering due to changes in atomic coordinates have not been included. The green horizontal shading represents the uncertainty in the experimental value of the ionization energy of the singlet ground state [86]. The results obtained with the r^{2}SCAN underestimate the experimental ZPL triplet energy by only 0.15 eV, while LDA has the largest error (0.27 eV). The energy lowering due to relaxation of atomic coordinates in the singlet states has been estimated recently using spin-flip TDDFT calculations giving 0.06-0.1 eV for ^1E and 0.02 eV for $^1A_1$ [87]. Applying these corrections to the r^{2}SCAN values for the singlets gives ZPL energy of the singlet transition close to the experimental estimate, 1.19 eV, but underestimates the difference between the $^1A_1$ and ^3E excited states. The results using the TPSS functional provide a more accurate value of the $^1A_1 - {}^3E$ energy difference. [a]Ref. [85, 86, 88].

difference between the optimized geometry in the ^3E electronic state and the optimized geometry in the $^3A_2$ electronic state. The ZPL triplet energy that best agrees with the experiment is again obtained with the r^{2}SCAN XC functional and differs from the experimental ZPL by only -0.15 eV.

In conclusion, research question 5 in sec. 1.2 is answered:

Density functionals of the KS form can be used to model the negatively charged nitrogen-vacancy defect in diamond in very good agreement of the vertical excitation energies to high-level many-body methods and of the zero phonon line triplet energy to experimental results.

5 Conclusions

A direct optimization generalized mode following method has been presented and the performance of direct optimization methods has been assessed providing the following answers to the research questions posed in sec. 1.2:

1. Multiple emerging solutions in consecutive variational time-independent density functional calculations of excited electronic states at different positions of the nuclei can be differentiated by their saddle point orders on the surface defined by the electronic degrees of freedom. Based on the saddle point order, the desired solution can be targeted with the newly developed direct optimization generalized mode following method and variational collapse is prevented by construction.

2. Spurious solutions introduced by Perdew-Zunger self-interaction correction on the energy surface defined by the electronic degrees of freedom are characterized by maximizing the self-interaction error along some electronic degrees of freedom. A strategy is presented to avoid such spurious solutions with the generalized mode following method by performing a minimization in the subspace of occupied-occupied orbital rotation degrees of freedom and following only those eigenvectors of the electronic Hessian up in energy that are localized in the subspace of occupied-virtual orbital rotation degrees of freedom.

3. Direct optimization methods can provide the correct topology of a conical intersection in the ethylene molecule provided that the single-determinant wave functions are allowed to break the symmetries of the Hamiltonian.

4. Variational time-independent direct orbital optimization methods outperform linear-response time-dependent density functional theory in calculations of the excitation energy of charge transfer states

of organic molecules. While the time-dependent calculations tend to perform more poorly the larger the extend of charge transfer of the excited state, no such correlation is observed for the variational methods.

5. Density functionals of the KS form can be used to model the negatively charged nitrogen-vacancy defect in diamond in very good agreement of the vertical excitation energies to high-level many-body methods and of the zero phonon line triplet energy to experimental results.

References

[1]V. Balzani, G. Bergamini, and P. Ceroni, "Light: A Very Peculiar Reactant and Product," Angew. Chem., Int. Ed. **54**, 11320–11337 (2015).

[2]E. Romero, V. I. Novoderezhkin, and R. V. Grondelle, "Quantum design of photosynthesis for bio-inspired solar-energy conversion," Nature **543**, 355–365 (2017).

[3]N. Armaroli and V. Balzani, "Solar Electricity and Solar Fuels: Status and Perspectives in the Context of the Energy Transition," Chem. Eur. J. **22**, 32–57 (2016).

[4]W. Shockley and H. J. Queisser, "Detailed balance limit of efficiency of p-n junction solar cells," J. Appl. Phys. **32**, 510–519 (1961).

[5]M. B. Smith and J. Michl, "Singlet fission," Chem. Rev. **110**, 6891–6936 (2010).

[6]V. Gray, K. Moth-Poulsen, B. Albinsson, and M. Abrahamsson, "Towards efficient solid-state triplet–triplet annihilation based photon upconversion: Supramolecular, macromolecular and self-assembled systems," Coord. Chem. Rev. **362**, 54–71 (2018).

[7]N. Mariotti, M. Bonomo, L. Fagiolari, N. Barbero, C. Gerbaldi, F. Bella, and C. Barolo, "Recent advances in eco-friendly and cost-effective materials towards sustainable dye-sensitized solar cells," Green Chem. **22**, 7168–7218 (2020).

[8]T. Helgaker, P. Jørgensen, and J. Olsen, *Molecular Electronic Structure Theory*, Vol. 1 (Wiley, 2000).

[9]F. Jensen, *Introduction to Computational Chemistry*, Vol. 3 (2017).

[10]A. Szábo and S. O. Neil, *Modern Quantum Chemistry*, Vol. 1 (1989).

[11]P. Hohenberg and W. Kohn, "Inhomogeneous Electron Gas," Phys. Rev. **136**, B864–B871 (1964).

[12]W. Kohn and L. J. Sham, "Self-Consistent Equations Including Exchange and Correlation Effects," Phys. Rev. A **140**, A1133–A1138 (1965).

[13]E. Runge and E. K. U. Gross, "Density-Functional Theory for Time-Dependent Systems," Phys. Rev. Lett. **52**, 997 (1984).
[14]M. A. L. Marques, N. T. Maitra, F. M. S. Nogueira, E. K. U. Gross, and A. Rubio, *Fundamentals of time-dependent density functional theory*, Vol. 837 (Springer, 2012).
[15]M. E. Casida, "Time-Dependent Density Functional Response Theory for Molecules," in *Recent Advances in Computational Chemistry* (1995), pp. 155–192.
[16]B. G. Levine, C. Ko, J. Quenneville, and T. J. Martínez, "Conical intersections and double excitations in time-dependent density functional theory," Mol. Phys. **104**, 1039–1051 (2006).
[17]Y. Shao, M. Head-Gordon, and A. I. Krylov, "The spin-flip approach within time-dependent density functional theory: Theory and applications to diradicals," J. Chem. Phys. **118**, 4807–4818 (2003).
[18]N. T. Maitra, F. Zhang, R. J. Cave, and K. Burke, "Double excitations within time-dependent density functional theory linear response," J. Chem. Phys. **120**, 5932–5937 (2004).
[19]N. T. Maitra, "Charge transfer in time-dependent density functional theory," J. Phys. Condens. Matter **29**, 423001 (2017).
[20]Y. Shu, K. A. Parker, and D. G. Truhlar, "Dual-Functional Tamm-Dancoff Approximation: A Convenient Density Functional Method that Correctly Describes S1/S0 Conical Intersections," J. Phys. Chem. Lett. **8**, 2107–2112 (2017).
[21]Y. Shu, K. A. Parker, and D. G. Truhlar, "Dual-functional Tamm-Dancoff approximation with self-interaction-free orbitals: vertical excitation energies and potential energy surfaces near an intersection seam," J. Phys. Chem. **121**, 9728–9735 (2017).
[22]L. Lacombe and N. T. Maitra, "Non-adiabatic approximations in time-dependent density functional theory: progress and prospects," Npj Comput. Mater. **9**, 124 (2023).
[23]G. Levi, A. V. Ivanov, and H. Jónsson, "Variational calculations of excited states via direct optimization of the orbitals in DFT," Faraday Discuss. **224**, 448–466 (2020).
[24]G. Levi, A. V. Ivanov, and H. Jónsson, "Variational density functional calculations of excited states via direct optimization," J. Chem. Theory Comput. **16**, 6968–6982 (2020).
[25]A. V. Ivanov, G. Levi, E. Ö. Jónsson, and H. Jónsson, "Method for Calculating Excited Electronic States Using Density Functionals and

Direct Orbital Optimization with Real Space Grid or Plane-Wave Basis Set," J. Chem. Theory Comput. **17**, 5034–5049 (2021).
[26]D. Hait and M. Head-Gordon, "Orbital Optimized Density Functional Theory for Electronic Excited States," J. Phys. Chem. Lett. **12**, 4517–4529 (2021).
[27]M. Head-Gordon and J. A. Pople, "Optimization of Wave Function and Geometry in the Finite Basis Hartree-Fock Method," J. Phys. Chem **92**, 3063–3069 (1988).
[28]F. Neese, "Approximate second-order SCF convergence for spin unrestricted wavefunctions," Chem. Phys. Lett. **325**, 93–98 (2000).
[29]T. Van Voorhis and M. Head-Gordon, "A geometric approach to direct minimization," Mol. Phys. **100**, 1713–1721 (2002).
[30]J. VandeVondele and J. Hutter, "An efficient orbital transformation method for electronic structure calculations," J. Chem. Phys. **118**, 4365–4369 (2003).
[31]A. V. Ivanov, E. Jónsson, T. Vegge, and H. Jónsson, "Direct energy minimization based on exponential transformation in density functional calculations of finite and extended systems," Comput. Phys. Commun. **267**, 108047 (2021).
[32]H. G. Burton, "Energy Landscape of State-Specific Electronic Structure Theory," J. Chem. Theory Comput. **18**, 1512–1526 (2022).
[33]J. J. Mortensen, A. H. Larsen, M. Kuisma, A. V. Ivanov, A. Taghizadeh, A. Peterson, A. Haldar, A. O. Dohn, C. Schäfer, E. Ö. Jónsson, E. D. Hermes, F. A. Nilsson, G. Kastlunger, G. Levi, H. Jónsson, H. Häkkinen, J. Fojt, J. Kangsabanik, J. Sødequist, J. Lehtomäki, J. Heske, J. Enkovaara, K. T. Winther, M. Dulak, M. M. Melander, M. Ovesen, M. Louhivuori, M. Walter, M. Gjerding, O. Lopez-Acevedo, P. Erhart, R. Warmbier, R. Würdemann, S. Kaappa, S. Latini, T. M. Boland, T. Bligaard, T. Skovhus, T. Susi, T. Maxson, T. Rossi, X. Chen, Y. L. A. Schmerwitz, J. Schiøtz, T. Olsen, K. W. Jacobsen, and K. S. Thygesen, "GPAW: An open Python package for electronic structure calculations," J. Chem. Phys. **160**, 092503 (2024).
[34]G. Onida, L. Reining, and A. Rubio, "Electronic excitations: density-functional versus many-body Green's-function approaches," Rev. Mod. Phys. **74**, 601–659 (2002).
[35]J. P. Perdew and Y. Wang, "Accurate and simple analytic representation of the electron-gas correlation energy," Phys. Rev. B **45**, 13244 (1992).

[36]M. Levy, "Universal variational functionals of electron densities, first-order density matrices, and natural spin-orbitals and solution of the v-representability problem," Phys. **76**, 6062–6065 (1979).
[37]J. P. Perdew and A. Zunger, "Self-interaction correction to density-functional approximations for many-electron systems," Phys. Rev. B **23**, 5048–5079 (1981).
[38]J. E. Campbell, "On a Law of Combination of Operators bearing on the Theory of Continuous Transformation Groups," Proc. London Math. Soc. **s1–28**, 381–390 (1896).
[39]J. E. Campbell, "On a Law of Combination of Operators (Second Paper)," Proc. London Math. Soc. **s1–29**, 14–32 (1897).
[40]H. F. Baker, "Alternants and Continuous Groups," Proc. London Math. Soc. **2**, 24–47 (1905).
[41]F. Hausdorff, "Die symbolische Exponentialformel in der Gruppentheorie," Ber. Verh. Kgl. Sächs. Ges. Wiss. Leipzig., Math.-phys. Kl. **58**, 19–48 (1906).
[42]Y. Yamaguchi, I. L. AIberts, J. D. Goddard I, and H. F. Schaefer III, "Use of the molecular orbital Hessian for self-consistent-field (SCF) wavefunctions," Chem. Phys. **147**, 309–326 (1990).
[43]C. Moler and C. V. Loan, "Nineteen Dubious Ways to Compute the Exponential of a Matrix, Twenty-Five Years Later," Soc. Ind. Appl. Math. **45**, 3–49 (2003).
[44]A. H. Al-Mohy and N. J. Higham, "A new scaling and squaring algorithm for the matrix exponential," SIAM J. Matrix Anal. Appl. **31**, 970–989 (2009).
[45]T. P. Rossi, S. Lehtola, A. Sakko, M. J. Puska, and R. M. Nieminen, "Nanoplasmonics simulations at the basis set limit through completeness-optimized, local numerical basis sets," J. Chem. Phys. **142**, 094114 (2015).
[46]A. H. Larsen, M. Vanin, J. J. Mortensen, K. S. Thygesen, and K. W. Jacobsen, "Localized atomic basis set in the projector augmented wave method," Phys. Rev. B, Condens. Matter **80**, 195112 (2009).
[47]J. P. Perdew, K. Burke, and M. Ernzerhof, "Generalized Gradient Approximation Made Simple," Phys. Rev. Lett. **77**, 3865 (1996).
[48]J. P. Perdew, K. Burke, and M. Ernzerhof, "Erratum: Generalized Gradient Approximation Made Simple," Phys. Rev. Lett. **78**, 1396 (1997).

[49]J. Nocedal and S. J. Wright, *Numerical Optimization*, edited by T. V. Mikosch, S. M. Robinson, and S. I. Resnick, 2nd ed., Vol. 2 (Springer, 2006).
[50]J. Nocedal, "Updating quasi-Newton matrices with limited storage," Math. Comput. **35**, 773–782 (1980).
[51]D. C. Liu and J. Nocedal, "On the limited memory BFGS method for large scale optimization," Math. Prog. **45**, 503–528 (1989).
[52]B. A. Murtagh and R. W. H. Sargent, "Computational experience with quadratically convergent minimisation methods," Comput. J. **13**, 185–194 (1970).
[53]M. J. D. Powell, "A New Algorithm for Unconstrained Optimization," Nonlinear Prog., 31–65 (1973).
[54]J. M. Bofill, "Updated Hessian Matrix and the Restricted Step Method for Locating Transition Structures," J. Comput. Chem. **15**, 1–11 (1994).
[55]A. T. B. Gilbert, N. A. Besley, and P. M. W. Gill, "Self-Consistent Field Calculations of Excited States Using the Maximum Overlap Method (MOM)," J. Phys. Chem. **112**, 13164–13171 (2008).
[56]G. M. J. Barca, A. T. B. Gilbert, and P. M. W. Gill, "Simple Models for Difficult Electronic Excitations," J. Chem. Theory Comput. **14**, 1501–1509 (2018).
[57]G. Henkelman and H. Jónsson, "A dimer method for finding saddle points on high dimensional potential surfaces using only first derivatives," J. Chem. Phys. **111**, 7010–7022 (1999).
[58]R. A. Olsen, G. J. Kroes, G. Henkelman, A. Arnaldsson, and H. Jónsson, "Comparison of methods for finding saddle points without knowledge of the final states," J. Chem. Phys. **121**, 9776–9792 (2004).
[59]J. Kästner and P. Sherwood, "Superlinearly converging dimer method for transition state search," J. Chem. Phys. **128**, 014106 (2008).
[60]M. P. Gutiérrez, C. Argáez, and H. Jónsson, "Improved Minimum Mode Following Method for Finding First Order Saddle Points," J. Chem. Theory Comput. **13**, 125–134 (2016).
[61]E. Wigner, "The transition state method," Trans. Faraday Soc. **34**, 29–41 (1938).
[62]G. H. Vineyard, "Frequency factors and isotope effects in solid state rate processes," J. Phys. Chem. Solids **3**, 121–127 (1957).
[63]E. R. Davidson, "The iterative calculation of a few of the lowest eigenvalues and corresponding eigenvectors of large real-symmetric matrices," J. Comput. Phys. **17**, 87–94 (1975).

[64]M. Crouzeix, B. Philippe, and M. Sadkane, "The Davidson Method," SIAM J. Sci. Comput. **15**, 62–76 (1994).
[65]T. H. Dunning, "Gaussian basis sets for use in correlated molecular calculations. I. The atoms boron through neon and hydrogen," J. Chem. Phys. **90**, 1007–1023 (1989).
[66]R. A. Kendall, T. H. Dunning, and R. J. Harrison, "Electron affinities of the first-row atoms revisited. Systematic basis sets and wave functions," J. Chem. Phys. **96**, 6796–6806 (1992).
[67]D. E. Woon and T. H. Dunning, "Gaussian basis sets for use in correlated molecular calculations. IV. Calculation of static electrical response properties," J. Chem. Phys. **100**, 2975–2988 (1994).
[68]M. Barbatti and R. Crespo-Otero, "Surface Hopping Dynamics with DFT Excited States," in *Density-Functional Methods for Excited States*, edited by N. Ferré, M. Filatov, and M. Huix-Rotllant (Springer International Publishing, 2016), pp. 415–444.
[69]E. Pradhan, K. Sato, and A. V. Akimov, "Non-adiabatic molecular dynamics with ΔSCF excited states," J. Phys. Condens. Matter **30**, 484002 (2018).
[70]A. D. Becke, "Density-functional exchange-energy approximation with correct asymptotic behavior," Phys. Rev. A **38**, 3098–3100 (1988).
[71]C. Lee, W. Yang, and R. G. Parr, "Development of the Colle-Salvetti correlation-energy formula into a functional of the electron density," Phys. Rev. B **37**, 785–789 (1988).
[72]T. Le Bahers, C. Adamo, and I. Ciofini, "A qualitative index of spatial extent in charge-transfer excitations," J. Chem. Theory Comput. **7**, 2498–2506 (2011).
[73]P.-F. Loos, M. Comin, X. Blase, and D. Jacquemin, "Reference energies for intramolecular charge-transfer excitations," J. Chem. Theory Comput. **17**, 3666–3686 (2021).
[74]P. J. Stephens, F. J. Devlin, C. S. Ashvar, C. F. Chabalowski, and M. J. Frisch, "Theoretical calculation of vibrational circular dichroism spectra," Faraday Discuss. **99**, 103–119 (1994).
[75]A. D. Becke, "Density-functional thermochemistry. III. The role of exact exchange," J. Chem. Phys. **98**, 5648–5652 (1993).
[76]T. Yanai, D. P. Tew, and N. C. Handy, "A new hybrid exchange-correlation functional using the Coulomb-attenuating method (CAM-B3LYP)," Chem. Phys. Lett. **393**, 51–57 (2004).

[77]H. Ma, M. Govoni, and G. Galli, "Quantum simulations of materials on near-term quantum computers," Npj Comput. Mater. **6**, 85 (2020).
[78]M. Bockstedte, F. Schütz, T. Garratt, V. Ivády, and A. Gali, "Ab initio description of highly correlated states in defects for realizing quantum bits," Npj Quantum Mater. **3**, 31 (2018).
[79]S. Choi, M. Jain, and S. G. Louie, "Mechanism for optical initialization of spin in NV-center in diamond," Phys. Rev. B **86**, 041202 (2012).
[80]Y. Ma, M. Rohlfing, and A. Gali, "Excited states of the negatively charged nitrogen-vacancy color center in diamond," Phys. Rev. B **81**, 041204 (2010).
[81]C. Bhandari, A. L. Wysocki, S. E. Economou, P. Dev, and K. Park, "Multiconfigurational study of the negatively charged nitrogen-vacancy center in diamond," Phys. Rev. B **103**, 014115 (2021).
[82]J. Tao, J. P. Perdew, V. N. Staroverov, and G. E. Scuseria, "Climbing the Density Functional Ladder: Nonempirical Meta–Generalized Gradient Approximation Designed for Molecules and Solids," Phys. Rev. Lett. **91**, 146401 (2003).
[83]J. W. Furness, A. D. Kaplan, J. Ning, J. P. Perdew, and J. Sun, "Accurate and Numerically Efficient r2SCAN Meta-Generalized Gradient Approximation," J. Phys. Chem. Lett. **11**, 8208–8215 (2020).
[84]V. M. Acosta, A. Jarmola, E. Bauch, and D. Budker, "Optical properties of the nitrogen-vacancy singlet levels in diamond," Phys. Rev. B **82**, 2–5 (2010).
[85]L. J. Rogers, S. Armstrong, M. J. Sellars, and N. B. Manson, "Infrared emission of the NV centre in diamond: Zeeman and uniaxial stress studies," New J. Phys. **10**, 103024 (2008).
[86]S. Wolf, I. Meirzada, G. Haim, and N. Bar-Gill, "Nitrogen-vacancy singlet manifold ionization energy," Phys. Rev. Appl. **19**, 034076 (2023).
[87]Y. Jin, M. Govoni, and G. Galli, "Vibrationally resolved optical excitations of the nitrogen-vacancy center in diamond," Npj Comput. Mater. **8**, 1–9 (2022).
[88]G. Davies and M. F. Hamer, "Optical studies of the 1.945 eV vibronic band in diamond," Proc. R. Soc. A **348**, 285–298 (1976).

Appendix A: Related Publications

Alec E. Sigurðarson, **Yorick L. A. Schmerwitz**, Dagrún K. V. Tveiten, Gianluca Levi, Hannes Jónsson, 2023, Orbital-optimized density functional calculations of molecular Rydberg excited states with real space grid representation and self-interaction correction. *The Journal of Chemical Physics*, Vol. 159, Issue 21, p. 214109.

Jens J. Mortensen, Ask H. Larsen, Mikael Kuisma, Aleksei V. Ivanov, Alireza Taghizadeh, Andrew Peterson, Anubhab Haldar, Asmus O. Dohn, Christian Schäfer, Elvar Ö. Jónsson, Eric D. Hermes, Fredrik A. Nilsson, Georg Kastlunger, Gianluca Levi, Hannes Jónsson, Hannu Häkkinen, Jakub Fojt, Jiban Kangsabanik, Joachim Sødequist, Jouko Lehtomäki, Julian Heske, Jussi Enkovaara, Kirsten T. Winther, Marcin Dulak, Marko M. Melander, Martin Ovesen, Martti Louhivuori, Michael Walter, Morten Gjerding, Olga Lopez-Acevedo, Paul Erhard, Robert Warmbier, Rolf Würdemann, Sami Kaappa, Simone Latini, Tara M. Boland, Thomas Bligaard, Thorbjørn Skovhus, Toma Susi, Tristan Maxson, Tuomas Rossi, Xi Chen, **Yorick L. A. Schmerwitz**, Jakob Schiøtz, Thomas Olsen, Karsten W. Jacobsen, Kristian S. Thygesen, 2024, GPAW: An open Python package for electronic structure calculations. *The Journal of Chemical Physics*, Vol. 160, Issue 9, p. 092503.

Original Article I

Calculations of Excited Electronic States by Converging on Saddle Points Using Generalized Mode Following

Y. L. A. Schmerwitz, G. Levi, H. Jónsson

Journal of Chemical Theory and Computation, 19, 3634–3651

Reprinted with permission from Journal of Chemical Theory and Computation. Copyright 2024 American Chemical Society.

Yorick Leonard Adrian Schmerwitz came up with the generalization of the algorithm used and described in the article, implemented the algorithm, performed calculations, created figures, and wrote the article.

Original Article II

Saddle Point Search Algorithms for Variational Density Functional Calculations of Excited Electronic States with Self-Interaction Correction

Y. L. A. Schmerwitz, N. U. Ollé, G. Levi, H. Jónsson

Proceedings of the Platform for Advanced Scientific Computing Conference

This work is licensed under the Creative Commons Attribution 4.0 International License.

Yorick Leonard Adrian Schmerwitz came up with the extension of the algorithm used and described in the manuscript, implemented the algorithm, performed calculations, created figures, and wrote the article.

Original Article III

Variational Density Functional Calculations of Excited States: Conical Intersection and Avoided Crossing in Ethylene Bond Twisting

Y. L. A. Schmerwitz, A. V. Ivanov, E. Ö. Jónsson, H. Jónsson, G. Levi

The Journal of Physical Chemistry Letters, 13, 3990–3999

Reprinted with permission from The Journal of Physical Chemistry Letters. Copyright 2024 American Chemical Society.

Yorick Leonard Adrian Schmerwitz performed calculations, created figures, and wrote the article.

Original Article IV

Orbital-Optimized Versus Time-Dependent Density Functional Calculations of Intramolecular Charge Transfer Excited States

E. Selenius, A. E. Sigurðarson, Y. L. A. Schmerwitz, G. Levi

Journal of Chemical Theory and Computation, 20, 3809–3822

Reprinted with permission from Journal of Chemical Theory and Computation. Copyright 2024 American Chemical Society.

Yorick Leonard Adrian Schmerwitz implemented the algorithm used in the article and helped with calculations and writing the manuscript.

Original Article V

Electronic excitations of the charged nitrogen-vacancy center in diamond obtained using time-independent variational density functional calculations

A. V. Ivanov, Y. L. A. Schmerwitz, G. Levi, H. Jónsson

SciPost Physics, 15, 009

This work is licensed under the Creative Commons Attribution 4.0 International License.

Yorick Leonard Adrian Schmerwitz helped with calculations and writing the article.